

# Recent Progress and Perspectives of Thermally Drawn Multimaterial Fiber Electronics

Gabriel Loke, Wei Yan, Tural Khudiyev, Grace Noel, and Yoel Fink\*

Fibers are the building blocks of a broad spectrum of products from textiles to composites, and waveguides to wound dressings. While ubiquitous, the capabilities of fibers have not rapidly increased compared to semiconductor chip technology, for example. Recognizing that fibers lack the composition, geometry, and feature sizes for more functions, exploration of the boundaries of fiber functionality began some years ago. The approach focuses on a particular form of fiber production, thermal-drawing from a preform. This process has been used for producing single material fibers, but by combining metals, insulators, and semiconductors all within a single strand of fiber, an entire world of functionality in fibers has emerged. Fibers with optical, electrical, acoustic, or optoelectronic functionalities can be produced at scale from relatively easy-to-assemble macroscopic preforms. Two significant opportunities now present themselves. First, can one expect that fiber functions escalate in a predictable manner, creating the context for a “Moore’s Law” analog in fibers? Second, as fabrics occupy an enormous surface around the body, could fabrics offer a valuable service to augment the human body? Toward answering these questions, the materials, performance, and limitations of thermally drawn fibers in different electronic applications are detailed and their potential in new fields is envisioned.

## 1. Introduction

Fabrics are ubiquitous in their woven, non-woven, and knitted forms. They offer the unique ability to deliver intriguing properties in the solid state such as their high dynamic bending elasticity and stretchability while possessing high strength; large surface area while being lightweight; high breathability and permeability while still being thermally and chemically protective. They are also machine-washable and tear- and shrink-resistant. Beyond all of these physical properties, the mass production of fabrics is supported by a highly scalable manufacturing process which underlies their ubiquity. Indeed, what makes fabrics so useful is the ability to engineer their material composition and architecture across a hierarchy of length scales from the individual strand of a micrometer scale fiber, to their twisted collection, and finally to their patterned macroscale assembly extending across meters of surface area. This is the reason we find fabrics in products of different purposes,

ranging from diapers to the different forms of apparel such as jackets, shirts, socks, and jeans, and from bandages to items such as composites, bags, blankets, and cushions. Despite all of these developments, the basic functions of fabrics have not changed much since the dawn of civilization. Fabrics are still solely thought of as aesthetic physical objects, with little progress in their technological functions when compared to other fields such as communications and electronics. Since many of the qualities of fabrics are determined on the fiber- and yarn-level, it makes sense to examine what opportunities and challenges exist toward escalating the basic functions on the fiber- and yarn-level.

Looking into the timeline of fibers, the hallmark technological transformation in the use of fibers begins with the invention of optical fibers. Today, optical fibers are indispensable items utilized as telecommunication waveguides to send and receive enormous amounts of light data<sup>[1,2]</sup> over the kilometer length scale between countries. Enabling such applications is the intrinsic advantages derived from the 1D structure of an optical fiber, including its high flexibility even as brittle materials such as silica are incorporated, its long length to enable large-distance implementation, and its thin structure. Beyond telecommunication, its long-length advantage is applicable for other fields such as civil engineering, where they are placed

G. Loke, Dr. W. Yan, Dr. T. Khudiyev, Prof. Y. Fink  
Research Laboratory of Electronics  
Massachusetts Institute of Technology  
Cambridge, MA 02139, USA  
E-mail: yoel@mit.edu

G. Loke, Prof. Y. Fink  
Institute of Soldier Nanotechnology  
Massachusetts Institute of Technology  
Cambridge, MA 02139, USA

G. Loke, Prof. Y. Fink  
Department of Materials Science and Engineering  
Massachusetts Institute of Technology  
Cambridge, MA 02139, USA

G. Noel  
Department of Chemical Engineering  
Massachusetts Institute of Technology  
Cambridge, MA 02139, USA

Prof. Y. Fink  
Department of Electrical Engineering and Computer Science  
Massachusetts Institute of Technology  
Cambridge, MA 02139, USA

Prof. Y. Fink  
Advanced Functional Fabrics of America (AFFOA)  
Cambridge, MA 02139, USA

 The ORCID identification number(s) for the author(s) of this article can be found under <https://doi.org/10.1002/adma.201904911>.

DOI: 10.1002/adma.201904911

along bridges and pipelines to detect flaws,<sup>[3–6]</sup> while its thin diameter facilitates its utility in the medical industry toward minimally intrusive probing of internal organs,<sup>[7]</sup> and laser ablation of tumors.<sup>[8–10]</sup> However, until around a few decades ago, fiber research was mainly focused on optical-related applications with few breakthroughs toward electronic purposes. This is primarily because the material space for multimaterial fibers is still limited. The glassy materials used for optical fibers are brittle and of high-temperature characteristics, which not only require additional care in processing but also present a challenge in incorporating different material classes and establishing well-defined interfaces to constitute an electronic device. Henceforth, new methods, materials, composites, and approaches to form fibers with electronic functionalities were developed. To date, there are varying methods toward fabricating multimaterial fibers, including dip coating,<sup>[11]</sup> spray coating,<sup>[12]</sup> or deposition<sup>[13,14]</sup> of functional layers onto textiles/fibers, wet-<sup>[15]</sup> or electro-spinning,<sup>[16]</sup> and thermal-drawing.<sup>[17,18]</sup> Specifically, the unique advantage of the thermal-drawing technique is its ability to co-draw multiple materials, including metals, insulators, and semiconductors, to enable a wealth of in-fiber electronic devices of different functionalities (**Figure 1**)—from sensing optical,<sup>[19]</sup> thermal,<sup>[20]</sup> chemical,<sup>[21]</sup> and mechanical signals,<sup>[22]</sup> to actuation<sup>[23]</sup> and acoustic emission.<sup>[24]</sup> Importantly, the materials and architectures within thermally drawn fibers are tunable from micro- to nanoscale dimensions,<sup>[25,26]</sup> achieving novel and complex geometries at the required device length scale. In this review, due to the intriguing capabilities of thermal drawing, we focus mainly on the technique of the thermal-draw process, its advantages and limitations, its state-of-the-art electronics, and new functionalities that have yet to be explored by this technique.

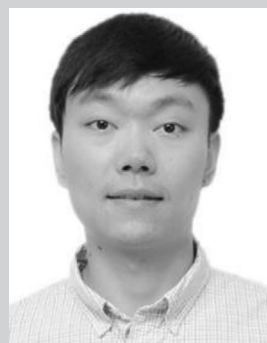
## 2. Description of the Thermal Drawing Process

The fabrication of optical fibers, meant for telecommunications, introduces the first-known process of thermal drawing.<sup>[27]</sup> Similar to the process of thermally drawing optical fibers, the first step toward fabricating a multimaterial electronic fiber is to prepare a preform. The preform is effectively an enlarged precursor of the fiber, and it is assembled with varying materials of desired shapes and structures (**Figure 2**). In the first type of multimaterial fibers originating back in 2002,<sup>[25,26]</sup> materials used are of low glass transition ( $T_g$ ), including thermoplastic polymers such as polycarbonate, or high  $T_g$  such as silica glass. It is necessary for all materials used within the preform to possess the same range of melting or glass transition temperatures for thermal co-drawing. For instance, a low melting point ( $T_m$ ) metallic core such as BiSn ( $T_m \approx 135^\circ\text{C}$ ) co-draws with a polycarbonate cladding which has a  $T_g$  of  $147^\circ\text{C}$ . Thermal co-drawing refers to the flow of two or more materials in a laminar fashion to enable a continuous fiber structure without any lumps or breakages arising from capillary instability.<sup>[28]</sup> It is noted that, while that the matching of these physical temperatures such as its  $T_g$  is commonly used, it is simply a guide toward knowing which materials can be combined together in a single preform draw. In actuality, matching the viscosities of



**Gabriel Loke** is currently a senior Ph.D. student in material science and engineering at the Massachusetts Institute of Technology (MIT) under the supervision of Prof. Yoel Fink. He earned his dual degree in physics and material science from National University of Singapore in 2015. His

research interests include the fabrication of novel multifunctional fibers for optoelectronic and computing applications, as well as the synergy between multimaterial fibers and additive manufacturing.



**Wei Yan** obtained his M.S. degree from Chinese Academy of Sciences in 2013 and Ph.D. degree from the Department of Materials Science and Engineering at the Ecole Polytechnique Fédérale de Lausanne (EPFL), Switzerland, 2017. Afterward he worked as a scientist at EPFL. In 2018, he joined the Research

Laboratory of Electronics, Massachusetts Institute of Technology (MIT), as a postdoc associate. His research interests focus on fiber-shaped flexible and stretchable electronics and optoelectronics for applications in sensing, energy harvesting, robotics, smart textiles, and neuroscience, as well as the fundamental study of in-fiber functional materials.



**Yoel Fink** is a professor of materials science and engineering and electrical engineering and computer science at the Massachusetts Institute of Technology (MIT). He previously served as the director of the Research Laboratory of Electronics and is currently serving as the Chief Executive Officer of the Advanced

Functional Fabrics of America (AFFOA). His research group at MIT works on the theory, design, fabrication, and characterization of multimaterial, multifunctional fibers, and fabrics.

## Thermally-drawn Multimaterial Fibers

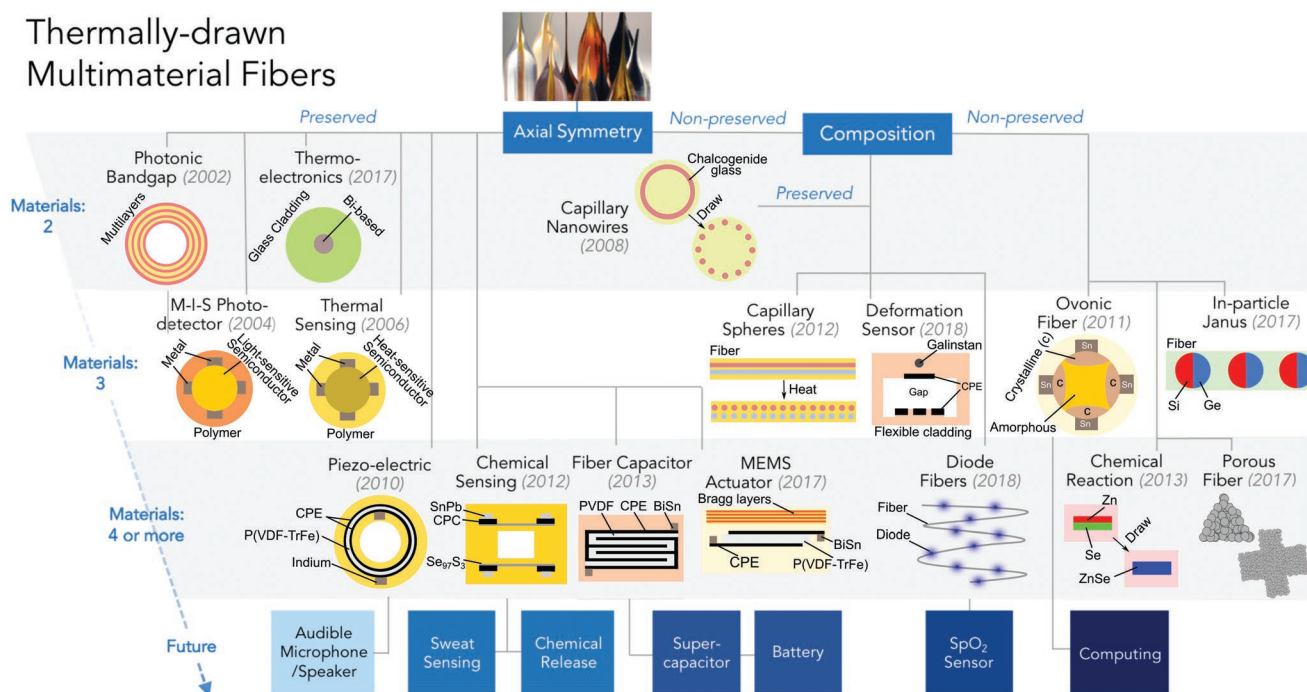


**Figure 1.** Timeline and roadmap of thermally drawn multimaterial fibers, which showcases the varying geometries, material compositions, and functionalities achieved in the past 20 years.

different materials is key toward ensuring that the materials co-draw. Another constraint is that the fiber cladding must be thermoplastic, rather than thermoset polymers.

The preparation of the individual material constituents within the preform involves different machining procedures such as milling, lathing, or laser cutting. These procedures allow for precise slots to be formed within the polymeric slabs, and for materials, including metals, to be constructed in different shapes and sizes and to be inserted into the preform. Shaping semiconductors requires alternative processing methods due to their brittle mechanical properties. To do so, semiconductor powder is usually consolidated within a hollow cylindrical tube in a heated rocking furnace, and then quenched to obtain a semiconductor cylinder rod. Alternatively, semiconductor thin films can be deposited on polymeric films via evaporative deposition and later wrapped around a polymeric cylinder. After manual assembly of all the components of the preform, a final thermal consolidation is typically done to merge the separated polymer slabs together into a single homogeneous preform.

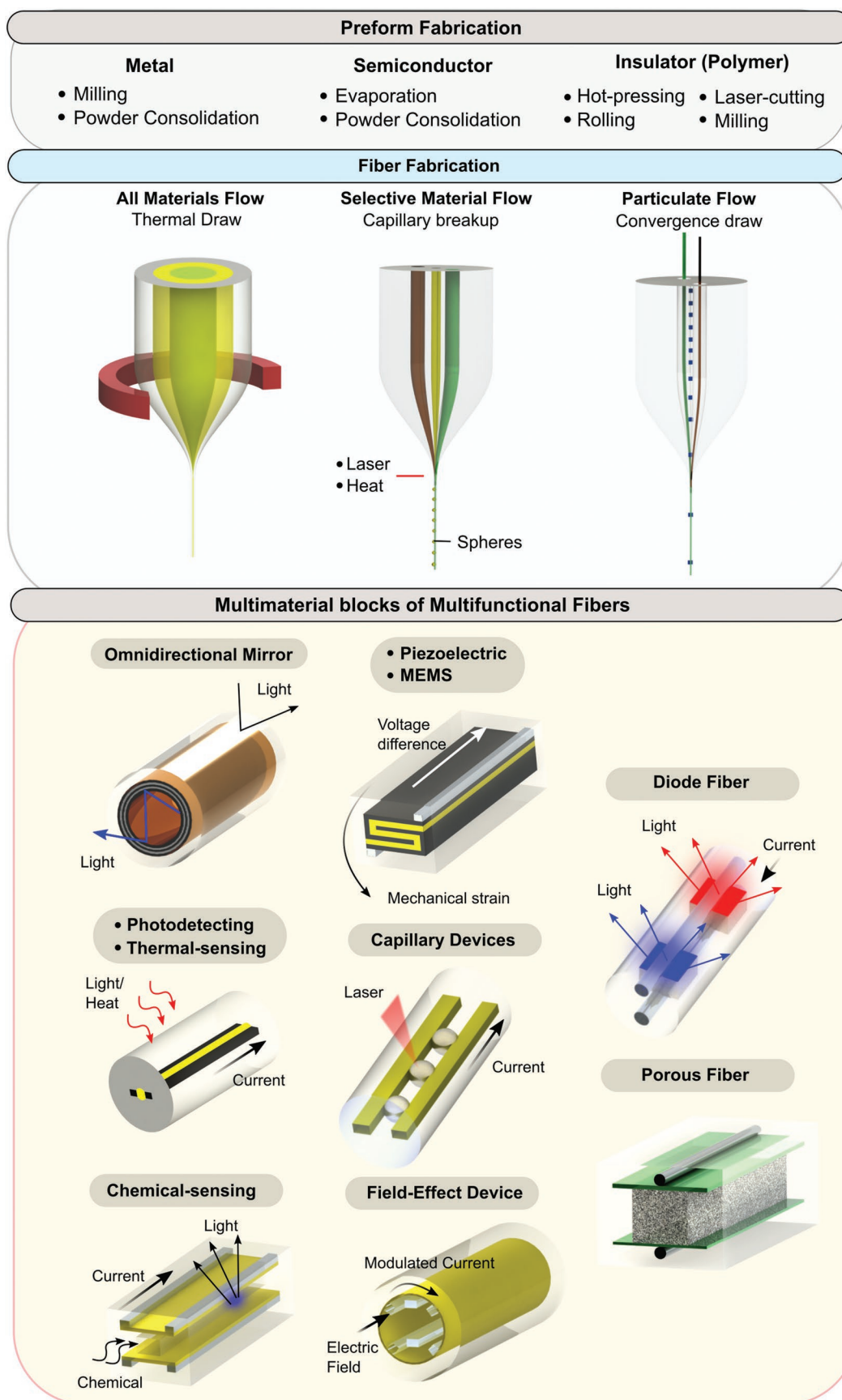
The multimaterial preform is then held in place within the furnace of a drawing tower, and the temperature is held at a value  $\approx 50\text{--}100\text{ }^{\circ}\text{C}$  higher than the  $T_g$  of the preform cladding. After a latency period of around 30 min to 1 h, the materials within the preform soften and undergo necking, facilitated by the pulling of a weight attached below the preform. The necking region is where the millimeter-wide multimaterial fiber is being pulled from the macroscopic preform. To enable continuous pulling, the fiber is drawn by a turning capstan with a speed ( $v_{\text{draw}}$ ), while the preform is fed downward into the furnace with a speed ( $v_{\text{feed}}$ ). Following the conservation of volume where the diameter of the preform is represented by  $D_{\text{preform}}$ ,

the diameter of the fiber ( $D_{\text{fiber}}$ ) decreases with the increase in  $v_{\text{draw}}$  according to the equation

$$D_{\text{fiber}} = D_{\text{preform}} \sqrt{\frac{v_{\text{feed}}}{v_{\text{draw}}}} \quad (1)$$

To increase the stress of the fiber draw so as to stabilize the fiber size, the temperature is typically decreased. Through this control in temperature and  $v_{\text{draw}}$ , fiber diameter in the range of 0.1–1 mm can be obtained while the internal fiber core materials can attain sizes down to the nanoscale with its cross-sectional structure translationally symmetric and continuous across kilometers of fiber length. Notably, material classes that are initially assembled within the preform now form intimate interfaces within the fiber to produce electrical junctions and dimensions necessary for operable devices.

In the second type of multimaterial fiber starting from the year 2012, a preform with continuous core materials is first formed into a fiber, similar to the first type of fiber as mentioned above. These fibers are characterized by their axially symmetric structure, where the fiber cross-section is identical throughout the length of the fiber, without the ability to tune or customize the structure at different positions along the fiber. Methods toward breaking these symmetries, in a postprocess manner after the fiber is drawn, are thus investigated, for example fragmentation or capillary breakup of fibers.<sup>[29,30]</sup> One of these methods (capillary breakup) is based on the Rayleigh instability phenomenon,<sup>[31]</sup> stating that a cylindrical core is metastable and the lowest energy shape is that of a sphere. As such, applying thermal agitation to fiber transforms the cylindrical fiber core into discrete





spheres. Thus far, such thermal agitation can be performed through three means: 1) placing the thermally drawn fiber into an oven or furnace which allows for the global transformation of materials within the fiber into thousands of spheres all at the same time,<sup>[29]</sup> 2) translating the fiber across a localized flame<sup>[32]</sup> which allows for controlled sphere formation, one at a time, from the feeding material core, and 3) using a laser which focuses on a particular material within the fiber to enable photothermal heating, hence local transformation into spheres.<sup>[33]</sup> Alternatively, to facilitate selective breakup of materials within the fiber, materials of different viscosity and size profiles can be incorporated in the fiber and by controlling the time and magnitude of heating, specific materials break up prior to others to form a fiber with both 0D spheres and 1D electrodes.<sup>[34]</sup>

Finally, in the third type of multimaterial fiber beginning in 2018,<sup>[35]</sup> prepackaged commercial microscale devices that are fabricated from silicon-based thin film technology are first prepared. Empty slots with dimensions similar to these discrete devices, as well as, channels for the wire electrodes, are milled from different polymeric preform slabs. The distance and size of these channels are calculated based on the desired fiber size and the draw-down ratio used. The devices are then placed manually into the empty slots of the preform slabs (automated methods for quick pick-and-place are currently being researched on). The different polymeric slabs are then assembled and consolidated together in a hot-press, with spacers preinserted into the wire channels of the preform to prevent their collapse during the heated consolidation. After consolidation, the devices are fully embedded and encapsulated within the volume of the preform with empty wire channels running along the length of the preform.

During the draw, highly conductive microwires acting as electrodes of width around 25–50  $\mu\text{m}$  thick, e.g., tungsten or copper, are fed into the preform. As the preform necks to form a fiber, the channels within the preform reduce in size until they match in dimension similar to the wire width. At this point, the polymer of the channel walls drags the wires down along with the fiber, aiding the unspooling of the wires from their individual spools. At the same time, as the preform transits into a fiber, the spacing between the device and wires are continuously reduced until the wires make eventual electrical contact with the devices. It is noted that these devices neither melt nor change in their performance when drawing. This interconnecting process, which we termed as “convergence,” highlights the converging of wires and devices together during the draw. We note that these microscale devices are akin to particles when compared to the macroscale preform, and only by understanding the rheology of the encapsulating polymer to control the flow of these

“particles” can we then enable their well positioning and hence high throughput interconnection between many of these devices and the wires. For example, too high of a stress value prevents the polymeric barrier between the wires and devices to break hence impeding contact between the wires and devices, while too small of a stress value results in more random flow perturbation of the polymer hence causing more discrete devices to be misaligned from the wires. The resultant 1D fiber contains a series of highly efficient micro-devices that are electrically addressed through the incorporated microwires.

Comparing the second and third types of fibers, both are identical, in that their fibers consist of both discrete (0D) and continuous (1D) structures. However, the process in forming these discrete entities in the fiber is different, as the second type of fiber makes use of postprocessing steps after thermal drawing whereas the third type of fiber introduces these discrete elements before the thermal draw. Looking ahead in terms of fabrication processes, it will be interesting to investigate the integration of the spherical breakup process used for the second type of fiber and the interconnection processes of discrete devices used for the third type of fiber. For example, spheres in fiber are similar to vertical vias in typical electrical circuits which connects two wires (top and bottom) together. As such, using this analogy, if spheres can be well arranged and positioned within the fiber, we anticipate the formation of an electrical circuit in fiber where different discrete devices along the fiber can be connected, in a customized fashion, to each other both through these vertical sphere “vias,” and horizontal wire electrodes.

### 3. Fiber Electronics in Sensing Applications

Creating fibers comprised of insulators, metals, and semiconductors poses unique fabrication challenges, but ultimately allows for an abundance of applications. This section describes some of the challenges with integrating metals and semiconductors into fibers and the techniques that can be used to fabricate these functional fibers. After laying out some of the fabrication details, this section explains important applications for the electronic fibers from optical interrogation to chemical and deformation sensing.

#### 3.1. Optoelectronic Fibers for Photosensing

The first strategy of making optoelectronic fibers relies on interfacing semiconductors with electrically conductive domains by exploiting the polymer fiber platform. Since the

**Figure 2.** Fabrication process toward forming the different multimaterial blocks of multifunctional fibers. Prior to drawing a fiber, several machining processes, including hot-pressing, film-rolling, semiconductor evaporation, stacking, and milling are first done to insert and assemble materials of different shapes into the preform. For the first type of fiber, the preform is assembled with co-drawable conductors, insulators, and semiconductors (i.e., materials that flow together) and is later drawn into a 1D, long, continuous device with micro or nanostructured features. In the second type of fiber, postprocessing steps such as laser or thermal annealing are performed to break the axial symmetric core into discontinuous, 0D capillary spherical devices. In the third type of fiber, discrete commercial devices are embedded into the preform with the feeding of microwires. During the draw, the devices and wires converge together to make electrical interconnects, forming a highly efficient device-integrated fiber. At the bottom of the figure, several multimaterial blocks of fibers are shown, depicting the varying geometries, materials, and functionalities that can be achieved from thermally drawn fibers.

process temperature is relatively low, chalcogenide semiconductors with low melting points or softening points are compatible with this process. Chalcogenide glass is formed based on the chalcogen elements S, Se, and Te or by the addition of other elements like As, Ge, Sn, Ga, etc. These glasses exhibit many unique optical properties, e.g., a wide range of transparency in the infrared, large refractive index, high nonlinearity, and low optical attenuation.<sup>[36–38]</sup> All these properties as well as thermal and crystallization properties, viscosity, absorption coefficient and optical bandgap are tunable depending on the composition. In particular, these glasses are very sensitive to irradiation in the visible range and can be easily processed at lower temperatures,<sup>[39–41]</sup> making them excellent for photodetecting applications within the polymer fiber platform.<sup>[42,43]</sup>

The first metal–semiconductor–insulator optoelectronic fiber fabricated by thermal drawing was demonstrated in 2004.<sup>[19,44]</sup> As shown in **Figure 3a**, the fiber was comprised of

an amorphous chalcogenide glass ( $\text{As}_{40}\text{Se}_{50}\text{Te}_{10}\text{Sn}_5$ ) core contacted by four metallic microwires and encapsulated by a transparent polymer cladding. Light incident on the fiber's external surface along the fiber length could be detected. These fibers were both highly flexible and mechanically tough, allowing them to be woven into fabrics that are capable of identifying the location of an illumination point.<sup>[19]</sup> Weaving these fibers into an optical array, web or a closed-surface sphere led to the measurement of amplitude and phase of an electromagnetic field over large areas,<sup>[45]</sup> as illustrated in **Figure 3b**. Another approach to localize the illumination points from the space was to break the axial symmetry through the construction of a convex electrical potential along the fiber axis.<sup>[46]</sup> **Figure 3c** shows the cross-section of such a fiber that integrates a bulk amorphous semiconducting core, a semiconducting thin film, as well as nanocomposite and metallic electrodes. The localization of an illumination point along 1 m of photodetecting fiber with a subcentimeter resolution was achieved.

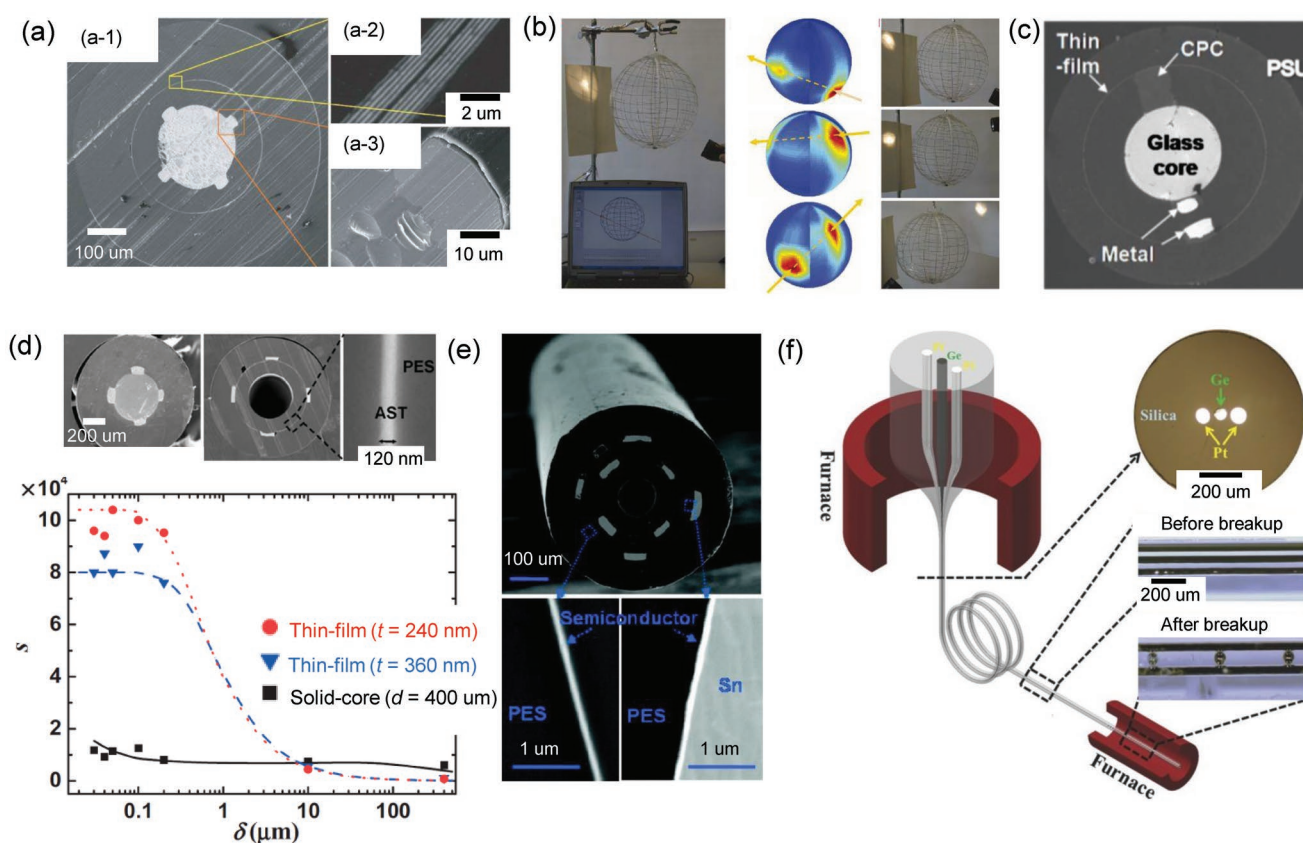


**Figure 3.** a) SEM micrograph of the cross-section of the first optoelectronic fiber consisting of a chalcogenide glass core interfaced by four metallic electrodes. The core region is surrounded by a photonic bandgap structure. Reproduced with permission.<sup>[19]</sup> Copyright 2004, Springer Nature. b) A closed spherical fiber web constructed by photodetecting fibers is an omnidirectional photodetector. It detects the direction of the beam throughout a solid angle of  $4\pi$ . Reproduced with permission.<sup>[45]</sup> Copyright 2006, Springer Nature. c) A photodetecting fiber that integrates a solid core consisting of metals, polymer composites and semiconductors, and a chalcogenide semiconductor thin film. It can distinguish optical illumination distributions (scale bar is not depicted in the referenced paper). Reproduced with permission.<sup>[46]</sup> Copyright 2010, OSA. d) SEM micrographs of the cross-section of a solid-core and a thin-film optoelectronic fiber. Comparison of the sensitivity for the solid-core and thin-film fiber as a function of penetration depth of the incident radiation. Reproduced with permission.<sup>[47]</sup> Copyright 2007, Wiley-VCH. e) SEM micrograph of an optoelectronic fiber with cascaded semiconducting thin-film configuration. Such fibers can sense light, its incoming direction, wavelength, and intensity. Reproduced with permission.<sup>[48]</sup> Copyright 2009, American Chemical Society. f) Schematic representation of the thermal drawing of a triple-core fiber and post-draw selective breakup process in a heating furnace. The resulting silica-cladding fiber contains one central semiconductor (germanium) core flanked by two metal (platinum) cores. Reproduced with permission.<sup>[50]</sup> Copyright 2016, Wiley-VCH.

Despite their photodetecting capabilities, the semiconductor cores in the aforementioned fibers are so bulky that electron/hole pairs can easily recombine by virtue of abundant traps in the materials, thereby limiting optoelectronic capabilities of these fibers. However, device performance can be improved by engineering the structure and geometry of the fiber. In particular, going from a bulky semiconductor core to a thin film configuration significantly improves the sensitivity of the photodetecting fiber,<sup>[47]</sup> as shown in Figure 3d.

Thanks to the miniaturized components, multiple optoelectronic devices can be integrated into a single fiber for more complex functionalities. Sorin et al.<sup>[48]</sup> demonstrated the successful integration of eight photodetecting devices with feature sizes as small as 100 nm into a single optoelectronic fiber (Figure 3e). This unique fiber is able to discriminate the wavelength in the visible range at a resolution below 5 nm and to measure the angle of incidence down to 4° angular resolution. Moreover, assembly of these single fibers into constructs or fabrics could not only localize spatial illumination points but could also image complex objects with polychromatic light non-interferometrically with no need for lenses.<sup>[38,48]</sup>

An alternative strategy involves thermally drawing semiconductors with high melting points, such as Si, Ge, or various compounds, within the silica glass fiber platform. The incorporation of these semiconductors into fibers enables new optoelectronic functionalities, extended transmission bands across the infrared spectral region, and potential for nonlinear optics in existing glass fiber technologies. The fibers are drawn at the softening temperature of silica, around 2000 °C, which is much higher than the melting points of these semiconductors. Interfacing semiconducting domains with electrodes remains a significant challenge. Because both components melt at such high temperatures, they will often intermix, which results in a loss of distinct electrical interfaces. Interconnections were thus made externally on both ends of the fibers for optoelectronic applications.<sup>[49]</sup> A recent approach to address this challenge relies on the selective breakup of the semiconductor core and built-in electrodes via in-fiber capillary instability. This strategy is illustrated in Figure 3f. A heating source is applied to the fiber to soften the glass cladding and subsequently induce breakup of the semiconductor wires. Simultaneously, the formed spheres push the softened silica aside to bridge the gap between two conductors, creating direct electrical connections between the crystalline semiconductor core and metal electrodes.<sup>[50]</sup> It should be noted that Plateau-Rayleigh capillary instability has been exploited to create microstructured semiconducting spheres<sup>[17,50–54]</sup> or well-ordered semiconducting nanowires<sup>[55,56]</sup> in fibers. Very recently, Deng and co-workers<sup>[57]</sup> developed a physical model and provide insight into the Plateau-Rayleigh capillary instability associated with breakup of semiconducting wires in thermally drawn fibers.

Another strategy for monolithic integration of metals and semiconductors in fibers is to exploit the high-pressure chemical vapor deposition (HPCVD) technique. Since different materials can be deposited sequentially, many unique devices such as Ohmic junctions, p–n junctions, Schottky junctions, and

p–i–n junctions can be fabricated within the silica glass fiber platform,<sup>[58–64]</sup> which are otherwise challenging to make by the thermal co-drawing technique.

## 3.2. Improving Device Performance of Optoelectronic Fibers

### 3.2.1. Crystallization of Optoelectronic Fibers

Both the as-drawn chalcogenide semiconductors in the multimaterial polymer fibers made via the thermal drawing approach and the deposited semiconductors in glassy silica fibers made via the HPCVD approach exhibit amorphous states. Amorphous semiconductors generally have a high density of shallow and deep traps in the energy gap. Electrons and holes interact with these traps when they drift through the energy gap, which reduces the drift mobility of charge carriers. Other localized states in the energy gap, such as valence alternation pair defects ( $\text{Se}^{3+}$  and  $\text{Se}^{1-}$ ) in Se, can reduce carrier lifetime (the average time it takes for a minority carrier to recombine). Furthermore, the carrier mean free path (defined as the average distance that a carrier can travel between scattering events) in amorphous semiconductors is short because they lack long-range order. Hence, carriers bump into disordered atoms randomly, resulting in their quick recombination. As a consequence, the disordered structure of semiconductors in these fibers is detrimental to their electronic and optoelectronic applications. For optical applications, the abundance of defects, such as the dangling bonds associated with the molecular disorder in amorphous Si, in these optical fibers creates a significant source of absorption, thereby reducing light transmission in the infrared range. In recent years, there have been tremendous efforts to induce crystallization of amorphous semiconductors in fibers. Controlling crystallinity, phase transformation, crystallographic orientation, and compositional segregation is of great importance for fabrication of high-performance optoelectronic devices and their exploitation for novel applications.<sup>[65,66]</sup>

### 3.2.2. Furnace-Based Annealing

The simplest and most straightforward way to induce crystallization is to thermally anneal the fibers above the glass-transition temperatures of semiconducting materials in a furnace. For the polymer fiber platform, it has been shown that thermal annealing is capable of improving responsivity or noise equivalent power for optoelectronic fibers<sup>[21,67,68]</sup> (Figure 4a) and increasing electrical mobility of a field-effect fiber.<sup>[69]</sup> For the silica fiber platform, one-step rapid photo-thermal processing applied to silicon optical fibers modifies local crystallinity and leads to ultralarge single crystal formation.<sup>[70–72]</sup> Multistep annealing approaches allow for an increase in the polycrystalline grain size and decrease in the dislocation defects in silicon optical fibers<sup>[73]</sup> or Se optical fibers.<sup>[74]</sup> Still, simple furnace-based thermal annealing results in the formation of polycrystalline semiconductors with a large number of grain boundaries, uncontrolled



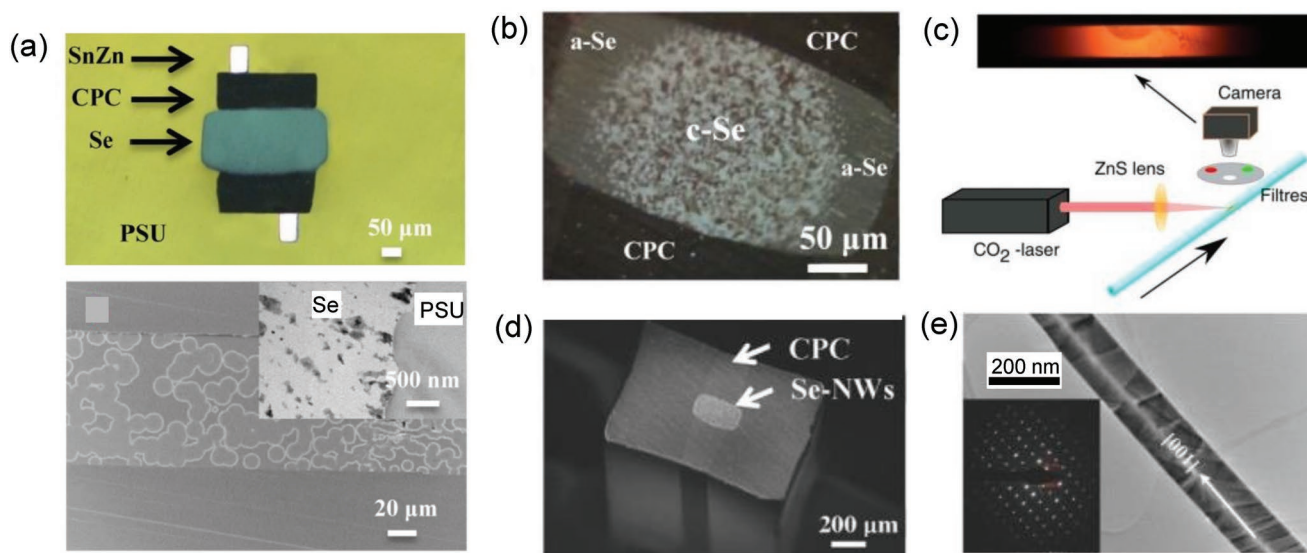


**Figure 4.** a) Top: Optical micrograph of an as-drawn optoelectronic fiber that contains a Se core; Bottom: Longitudinal section of a SEM micrograph of the annealed Se core. The inset is TEM characterization on the grain size. b) Optical micrograph of an optoelectronic fiber containing a Se core that was annealed by a laser. a,b) Reproduced with permission.<sup>[67]</sup> Copyright 2017, OSA. c) Schematic of the thermal drawing of a SiGe core optical fiber and its postannealing with a CO<sub>2</sub> laser recrystallization system. Reproduced under the terms of the CC-BY Creative Commons Attribution 4.0 International License (<http://creativecommons.org/licenses/by/4.0/>).<sup>[78]</sup> Copyright 2016, The Authors, published by Springer Nature. d) SEM image of the fiber cross-section after the formation of Se nanowire using a solution-based annealing approach. e) Transmission electron microscopy characterization on a single Se nanowire. The solvent modulates the anisotropy of the surface energy, favoring the growth of highly anisotropic crystals, elongated along their trigonal axis [001]. d,e) Reproduced with permission.<sup>[41]</sup> Copyright 2017, Wiley-VCH.

crystallization volume, and random crystallographic orientation.<sup>[68]</sup> Figure 4a (bottom) shows the microstructure of selenium along the longitudinal section of an optoelectronic fiber that was thermally annealed in a furnace. Nanoscale grains are clearly revealed by transmission electron microscopy imaging (the inset image). Although some additional strategies such as iterative drawing and tapering techniques have been coupled with thermal annealing,<sup>[75,76]</sup> these fibers still exhibit limited performance.

### 3.2.3. Laser-Based Annealing of Chalcogenide Semiconductors

A more powerful method of inducing crystallization is laser-based annealing. When the photon energy of a laser is larger than the bandgap energy of a semiconductor, the laser irradiation on the semiconductor generates heat, annealing the semiconductor. The laser-based annealing approach is able to accurately deliver high-density energy into a confined region because the photon penetration depth in the material is governed by the absorption coefficient. Heat generation during the laser treatment is thus limited to a very small depth that is, for example, 100 nm for amorphous Si at 400 nm, and 50 nm for amorphous Se at 500 nm.<sup>[77]</sup> Control over the crystallization volume of in-fiber semiconductors is always required to fabricate high-performance optoelectronic devices. Ideally, the crystallization depth would be just enough to absorb as much light as possible with the order of the penetration depth of the wavelength considered. Beyond this depth, crystalline domains would only result in noise, which is detrimental

to the sensitivity. In other words, if the crystallization depth can be controlled to be of the order of the photon penetration depth, light collection and charge extraction can be optimized to enable maximal photocurrent with minimal dark current, therefore resulting in high responsivity and sensitivity. Yan et al.<sup>[67]</sup> exploited a visible laser to anneal the amorphous Se core in an optoelectronic fiber and demonstrated that laser-based annealing could superiorly control phase transformation of the semiconductor core at the fiber tip. Thanks to a rapid heating process, the average grain size reached a few micrometers in the direction perpendicular to the electrodes, as shown by the cross-sectional optical micrograph in Figure 4b. Electron back scatter diffraction characterization on the crystallized Se core further confirmed the crystallinity. This drastically reduced the number of grain boundaries. The grain size was much smaller in the fiber axis direction, resulting in a shallow crystallization depth. Compared to fibers heat treated with a furnace-based approach, the fiber annealed with laser showed improved photoresponsivity and photosensitivity that was several orders of magnitude higher in a wide range of illumination power. Optoelectronic fibers with a functionalized tip may find several applications in highly sensitive remote detection and sensing, optoelectronic probes, minimally invasive in situ and in vivo biocompatible probing, and imaging of biological tissues.

### 3.2.4. Laser-Based Solidification of Group-IV-Based Semiconductors

It is clear that high-melting-point semiconductors, such as Si, Ge, and SiGe, in fiber form represent a large range of



potential scientific and technological advances. HPCVD provides a platform for depositing these semiconducting materials void-free with high-purity but with amorphous characteristics. Molten core thermal drawing, however, leads to polycrystalline semiconductors in fibers. Similar to the chalcogenide semiconductors, both amorphous and polycrystalline Group-IV-based semiconducting fibers exhibit high optical loss due to the defects in material structures. In addition to these two methods, the laser-based solidification approach has recently been demonstrated to have the unique capability of tailoring the composition, crystallinity, and grain size of the semiconductor core enabled by a well-controlled heating/cooling rate and thermal gradient. An impressive work, performed by Gibson's team, reported the fabrication of high-quality SiGe core with ultralarge grain size and uniform composition within silica fibers via laser-enabled remelting approach.<sup>[78]</sup> Figure 4c shows such a process. Typically, the SiGe-core of the as-drawn fiber is polycrystalline with a large number of grain boundaries and severe compositional variation that is detrimental to optical transmission in the infrared range. During the CO<sub>2</sub> laser treatment, a solidification velocity that is below the critical velocity predicted by the principle of constitutional supercooling is achieved by controlling the translation speed of the laser. This leads to compositional homogeneity in the core, as shown by the X-ray computed tomography characterization. The rapid translation of the melt zone and the large temperature gradients, present in the core at the same time, suppresses nucleation and crystallization at locations other than the advancing solidification front, which allows for the formation of large single crystals. Compositional gratings comprised of alternating Ge-rich regions and Si-rich regions can also be constructed by tailoring the crystallization conditions.<sup>[78]</sup> The versatility of this approach has been further demonstrated by re-solidifying other semiconductor cores. These include Si-core optical fibers with single crystals as large as 1.8 cm treated by CO<sub>2</sub> laser.<sup>[79]</sup> By using a 488 nm wavelength continuous wave laser, single crystal Si-core optical fibers up to 5.1 mm long and single crystal Ge-core optical fibers up to 9 mm long can be achieved.<sup>[80]</sup> Another recent study investigated the residual stress, bonding state at the interface between the Ge core and glass cladding, and optical loss of Ge-core optical fibers annealed by a CO<sub>2</sub> laser.<sup>[81]</sup> These fibers hold promise for applications in low-loss infrared waveguides for imaging spectroscopic endoscope, nonlinear optical devices at the mid-infrared, and integration with in-fiber Si photonic devices for photodetecting at the wavelength of 1.55  $\mu\text{m}$ .

### 3.2.5. Solution-Based Annealing

The formation of single crystal in-fiber semiconductors is highly desirable because of their defect-free characteristics. Recently, Yan et al.<sup>[41,82]</sup> reported a solution-based approach, in which individual atoms or molecules of a semiconductor are built up into 1D single crystals from seed nuclei for the integration of single crystal semiconducting nanowire-based optoelectronic devices into fibers. By controlling the anisotropy in

the surface energy of crystal planes, single crystal Se nanowires grow from the amorphous bulk in a solution to form direct intimate contact with built-in electrodes (Figure 4d). The nanowire growth mechanism was elucidated via electron microscopy as well as first-principles density-functional theory calculations. Figure 4e shows transmission electron microscopy characterization on a single nanowire, which reveals the crystal growth direction and crystallinity of such wires. The fiber devices exhibit unprecedented optical and optoelectronic performances, featuring high photoresponsivity and photosensitivity, low dark current, low noise-equivalent power, and ultrafast response speed, on par with many wafer-based devices. Most strikingly, this new approach facilitated high throughput and ultralarge area integration of nanowires into devices without the need for complex contacting procedures in the clean room, demonstrated by the growth of high-performance nanowire-based devices along the fiber length. Furthermore, they demonstrate the unique capability of a single fiber with hybrid functionalities—efficient optical guidance and excellent photodetecting performance—to enable fluorescent imaging.

In order to further understand the outstanding optoelectronic performance of devices, the charge carrier dynamics and mobility of the Se nanowire meshes were investigated by means of ultrafast transient absorption spectroscopy, nanosecond flash photolysis, and time-resolved terahertz spectroscopy.<sup>[83]</sup> These contact-free and noninvasive approaches revealed a lifetime on the picosecond scale for free carriers and on the microsecond scale for trapped carriers (both of which are limited by trap-assisted recombination) and a free carrier mobility of  $\approx 3.0 \text{ cm}^2 \text{ V}^{-1} \text{ s}^{-1}$ . The recovery time on the picosecond time scale of free carriers is attributed to ultrafast trapping of carriers mediated by surface states of each individual nanowire and contacts between nanowires because of the large surface to volume ratio of these randomly arranged wires. Nevertheless, the trapped carriers exhibiting long lifetimes on the microsecond scale can advance and be collected via hopping transport before they annihilate. This is beneficial for the use of Se nanowires in optoelectronic devices and is at the heart of the fiber-integrated device performance.<sup>[83]</sup> This work also reveals that the method for single crystal nanowire integration in the fiber platform can be extended to anisotropic fiber materials such as Te and Se/Te compound<sup>[84]</sup> that can be dissolved in corresponding solvents to exhibit an enhanced anisotropy of interfacial energy.

### 3.3. Optoelectronic Fibers for Remote Chemical Sensing

Toxic and hazardous gases or vapors are a serious threat to human health and the living environment, so capturing and sensing targeted chemicals is extremely important. In particular, luminescent-based detection provides unique advantages over other schemes in terms of instrumentation simplicity, portable implementation, and low cost. The typical luminescent-based approach relies on collecting and transmitting emission signals via an optical fiber to a photodetector at the distal end of the optical fiber. For example, Stolyarov et al.<sup>[85]</sup> demonstrated a hollow-channeled fiber

containing oxamide-based chemical agents that produce green luminescence upon reaction with the chemical of interest, peroxide vapor. The generated light traversed through the hollow optical channel for signal detection at the end of the fiber. Surrounding this optical waveguide is a photonic bandgap multilayered structure that decreases optical loss to the external environment. It was demonstrated that a minimum detected concentration of 100 ppb can be achieved from this fiber design. Nevertheless, optical transmission, bending losses, and coupling efficiency limit the minimum detected concentration.

To overcome this limitation, Gumennik et al.<sup>[21]</sup> developed an approach that monolithically integrates photodetecting elements flanking the hollow core of a polymer fiber where chemical vapors are circulated, as shown in Figure 5a. The inner surface of the hollow core is coated with a sensing material that chemically reacts with peroxide vapors flowing through the fiber core. The resulting chemiluminescent photons traverse through a transparent polymer and are captured by the fiber-embedded photodetectors. The high noise equivalent power of the amorphous  $\text{Se}_{97}\text{S}_3$ -based photodetectors preclude its use for chemiluminescent sensing, so the

fiber was thermally annealed in a furnace near the crystallization temperature of  $\text{Se}_{97}\text{S}_3$  for several hours. The device exhibits a sensitivity of  $0.176 \pm 0.005 \text{ nW ppm}^{-1}$  with a noise level of 0.517 nW, corresponding to a noise equivalent power of  $0.731 \text{ nW Hz}^{-0.5}$ . Optimizing chemiluminescent efficiency by placing the fiber system in a warm environment further enhances the performance, leading to detection of trace level of peroxide vapor down to 10 ppb (Figure 5b, left). Exploiting the crystallization scheme described in the previous section is expected to further improve the device performance. The photodetecting elements can extend along fibers that are hundreds of meters long, paving the way for remote and distributed chemical sensing, as illustrated in Figure 5b, right. Note that Se, Te, and their compounds acting as the fiber core have also been co-drawn with phosphate glasses for optoelectronic and optical applications.<sup>[64]</sup>

### 3.4. Electronic Fibers for Deformation Sensing

Functional fibers that sense deformation induced by pressure, bending, stretching, twisting, and shearing can enable a myriad

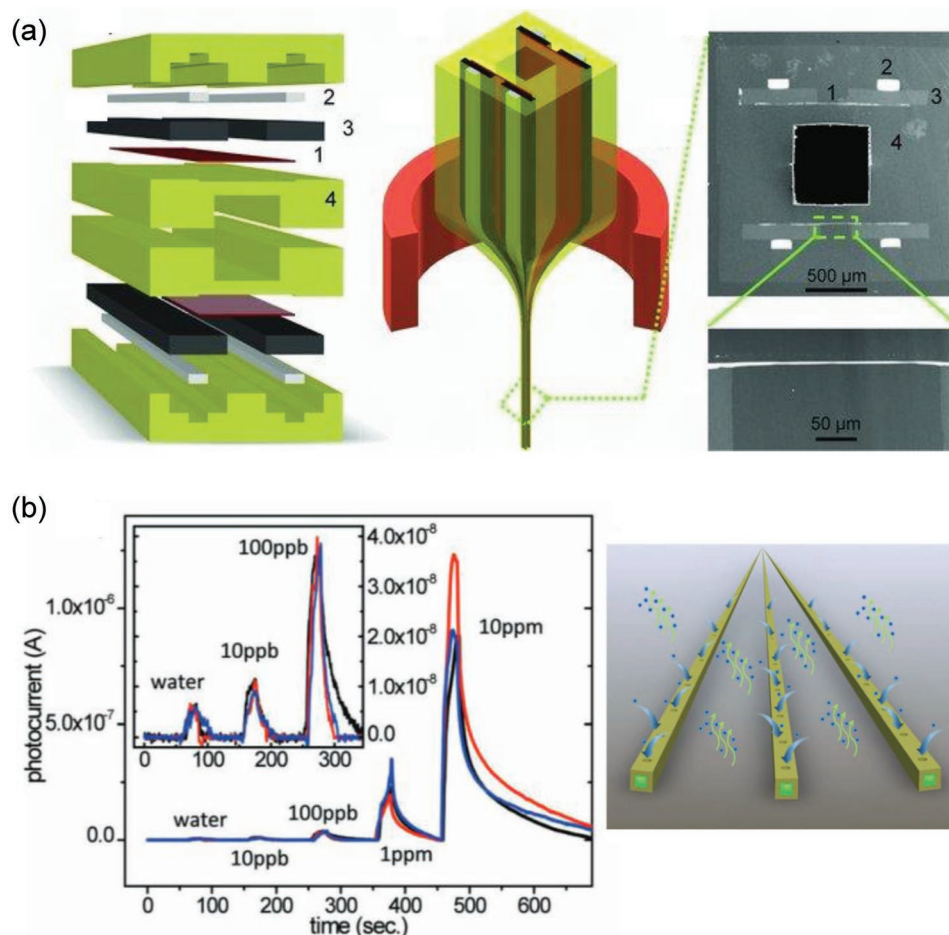


**Figure 5.** a) Schematic of thermal drawing of a chemical sensing fiber and the cross-sectional SEM micrograph showing the resulting fiber. The photo-detecting  $\text{Se}_{97}\text{S}_3$  layer is evaporated on the CPC electrodes. b) Left: Optoelectronic characterization on such fibers; Right: Concept schematic for remote and distributed sensing using such photodetecting fibers. a,b) Reproduced with permission.<sup>[21]</sup> Copyright 2012, Wiley-VCH.

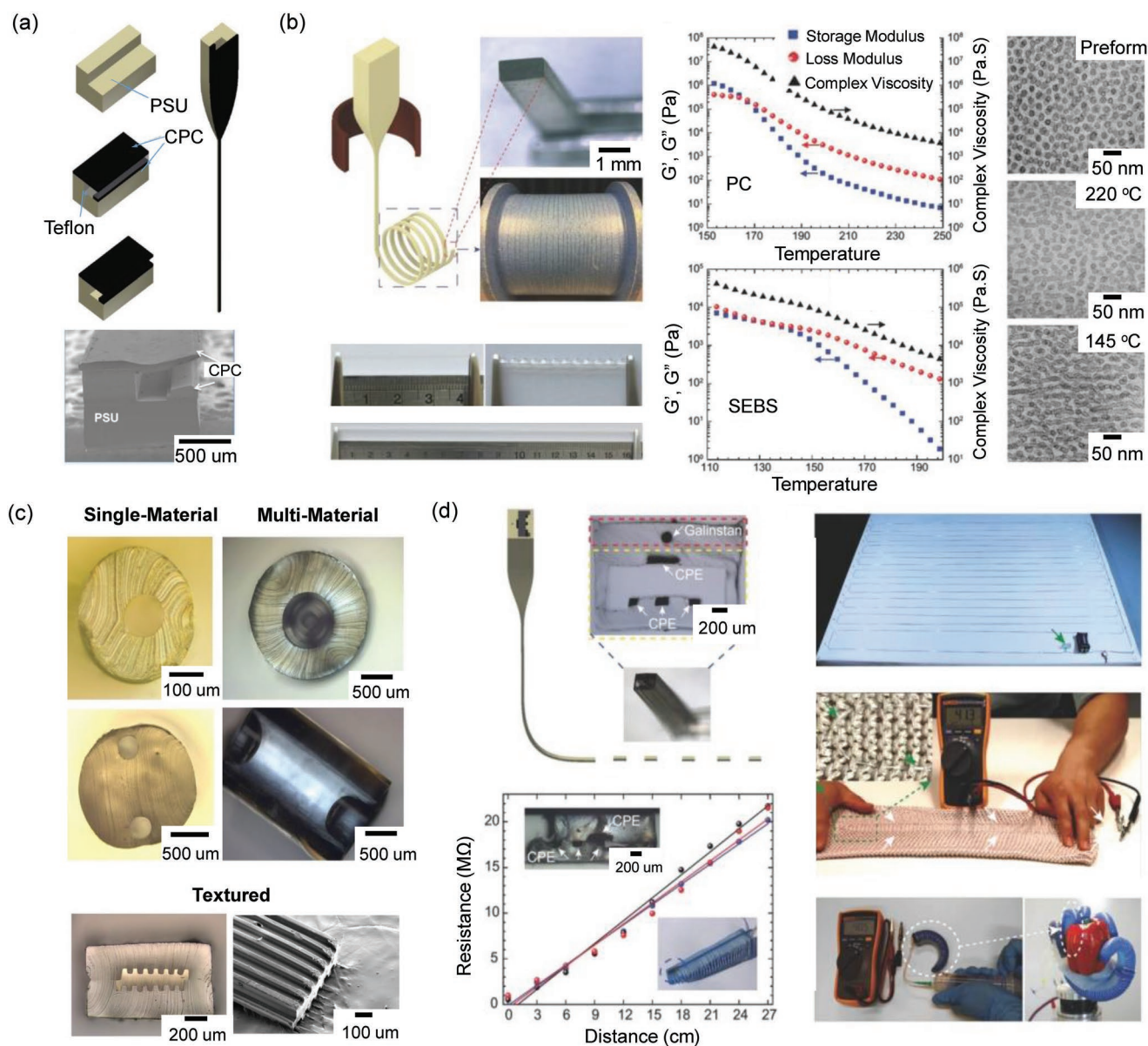


**Figure 6.** a) Multimaterial micro-electromechanical fibers with bendable functional domains. A cantilever-like design where a freestanding electrically conductive polymer composite film bends under an applied pressure into a micro-electromechanical fiber for press sensing. Reproduced with permission.<sup>[86]</sup> Copyright 2017, IOP Publishing. b) Left: Thermal drawing of stretchable and soft SEBS fibers. Middle: Shear viscosity measurement of a polycarbonate and a SEBS shows the similar rheological behavior. Right: TEM images of the SEBS before and after drawing at two different temperatures reveal the alignment of the hard phase (dark circles) when drawn at higher tension. Reproduced with permission.<sup>[87]</sup> Copyright 2018, Wiley-VCH. c) Microscopy images of food fibers that consist of gelatin [280 bloom]:glycerol 1:1 structure. Reproduced with permission.<sup>[93]</sup> Copyright 2019, Wiley-VCH. d) Pressure-sensing fibers and various applications of stretchable electronic fibers. Such fibers are integrated into a fabric, are cut into several short pieces of smaller networks or are positioned on the tip of robotic fingers to sense pressure and collect feedback information on the finger deformation. Reproduced with permission.<sup>[87]</sup> Copyright 2019, Wiley-VCH.

of applications in human motion monitoring, sports, tissue engineering, chronic disease detection, and human-machine interactions. Nguyen-Dang et al.<sup>[86]</sup> introduced a cantilever-like design in which a freestanding electrically conductive polymer composite film bends under an applied pressure into a micro-electromechanical fiber for compression sensing, as shown in **Figure 6a**. Mechanical touching leads to the bending of the conductive film, creating contacts with another electrically conducting domain underneath. The generated electrical signal

reveals the magnitude of the pressure exerted. This signal could be uniquely related to position along the fiber length at a submillimeter resolution by a judicious engineering of materials and electrical connectivity. The ability of a single fiber to simultaneously detect and localize pressure, as demonstrated here, is drastically different from the sensing strategies that utilize a complex 2D fabric mesh requiring numerous electrical connections. The fiber performance was unaltered after  $10^4$  loading cycles at 200 Hz. In addition, the fiber can recognize



and localize two pressure points, and exhibits a response bandwidth of close to 20 kHz.

The cladding of the abovementioned micro-electromechanical fiber is mechanically rigid, which makes sensing ultralow pressure very challenging. The integration of particular materials with complex architecture and functionalities within soft elastomeric claddings would be a major breakthrough. Despite decades of research however, elastomeric materials that can be used as fiber claddings in the field of thermal drawing have not been identified. Recently, a deep investigation of which materials constitute suitable elastic claddings through understanding their rheological properties has been performed by Prof. Fabien Sorin's group at the École Polytechnique Fédérale de Lausanne in Switzerland.<sup>[87–93]</sup> They first investigated the complex shear viscosity as well as the storage and loss moduli of some thermoplastics commonly used as claddings for thermal drawing. They discovered that a stable flow in the viscous regime can be identified by a temperature window in which the loss modulus changes slowly with temperature, crossing over the storage modulus that rapidly decreases, as shown by the rheological characterization in Figure 6b (middle). Based on this simple rheological criterion, a variety of thermoplastic elastomers that can be thermally drawn were discovered.

(Figure 6b, left). In particular, they identified poly(styrene-*b*-(ethylene-*co*-butylene)-*b*-styrene) (SEBS) copolymer with a high molecular weight and low hard phase content that meets the desired characteristic discussed above. The low hard phase (polystyrene) content of this elastomer leads to softening of the elastic network, corresponding to a rapid decrease of the storage modulus, while the high molecular weight ensures an elevated loss modulus during high viscosity flow. To further understand thermal drawing of thermoplastic elastomers, they performed transmission electron microscope analysis on the microstructure of the preform and its corresponding fibers along the drawing direction. It was discovered that the polystyrene spheres are distributed randomly within the soft matrix for the preform. At the fiber level, however, the polystyrene aggregates along the fiber drawing direction, forming elongated cylindrical domains due to their alignment in the preform neck-down region, as shown in Figure 6b, right. The aggregation of the hard phase in the fiber ensures a physical crosslinking when the material returns to room temperature from the neck-down region, resulting in preservation of the elasticity of the material after drawing. Furthermore, the same group has recently demonstrated the powerful platform of thermal drawing for the production of enjoyable yet healthy and nutritious food products by leveraging this simple rheological criterion.<sup>[93]</sup> Tailoring the content of the plasticizer and water in gelation, a common polymer in a variety of food products, results in suitable rheological properties required for thermal drawing. Hundreds of meters long gelation fibers with various shapes, surface textures, and integrated microchannel arrays were thus fabricated, as shown in Figure 6c. Nutrients could be filled within the channels of the fibers, and the digestion and release kinetics could be controlled to meet on-demand requirements. Being soft with an elastic modulus of a few tens of MPa, the plasticized gelation fiber is expected to deliver special applications in soft electronics.

The ability to integrate electronic functionalities into soft fibers opens novel opportunities for deformation sensing. Liquid metals, which provide an excellent combination of electrical conductivity and mechanical deformability, are compelling materials for thermally drawn soft electronics. Introducing one gallium wire within an SEBS fiber allows for the capability of elongation deformation detection by measuring the relative resistance change versus strain. The gauge factor of such an elongation sensor is comparable with the best liquid-metal-based sensors. Similarly, embedding two gallium wires into an SEBS fiber constitutes a different elongation sensor that functions by measuring relative capacitance change versus strain. Additionally, both the resistive and capacitive detection systems are sensitive to local pressure applied to the fiber. The resistive system measures a minimal force of 0.1 N while the capacitive system senses a force as low as 0.01 N, on par with the state of the art capacitive sensing devices. These fibers exhibit extraordinary mechanical robustness as demonstrated by the sustained conductivity and sensing ability after subjecting them to 10<sup>5</sup> stretching cycles. A variety of severe deformations such as twisting, shearing, or fast and large force impingement did not alter the mechanical attributes of these fibers. More complex functionalities were also demonstrated. A microstructured fiber integrated with a 3D assembly of a liquid metal electrode and four conducting polyethylene (CPE) electrodes in a hollow-core SEBS cladding (shown in Figure 6d, top left) was capable of measuring the magnitude of pressure, localizing its position along the fiber axis, and discriminating its direction in a plane perpendicular to the fiber axis. Such fibers could be used as long and soft interconnects or could be cut into several short pieces of smaller networks. They could be positioned on the tip of robotic fingers to sense pressure and collect sensitive feedback information on the finger deformation, as shown in Figure 6d. Indeed, deformation sensors with ultrahigh sensitivity hold unique applications in electronic skins,<sup>[94]</sup> artificial muscles,<sup>[95]</sup> soft robotics,<sup>[96]</sup> and detection of tumor tissue evolution.<sup>[97]</sup>

### 3.5. Other Electronic-Sensing Fibers

Assembling multiple fibers into arrays can create unprecedented functionalities like coherent interferences and beam steering. For instance, large-area acoustic fiber devices<sup>[22]</sup> pave the way toward novel applications in distributed pressure sensing, flow measurement, energy conversion, and communication transmission/reception. Another application associated with modulation from built-in electric fields in fibers is an azimuthally polarized radial fiber laser in which an array of electrically contacted liquid-crystal microchannels encircles the laser cavity in the fiber core. Applying an electric field modulates the polarized wavefront emanating from the core, leading to a laser with a dynamically controlled intensity distribution of full azimuthal angular range.<sup>[98]</sup> The integration of materials with multiple functionalities within single fibers increases their complexity. For example, Lv et al.<sup>[99]</sup> reports the realization of a nanostructured gallate glass in a multimaterial fiber capable of sensing temperature and pressure in a highly efficient way. Such progress represents a nice example of the development

of new fiber sensing materials by rational engineering of the structure units in noncrystalline solids.

### 3.6. Fiber as a Multimaterial Ink

Printing metals, insulators, and semiconductors together to form a device is challenging due to the mismatch in physical properties of these different material classes. Loke et al.<sup>[100]</sup> devised a new approach to utilize thermally drawn fibers as a 3D-printing feedstock toward constructing 3D optoelectronic devices. To enable the printing of these fibers, the authors made use of a print technique, which they coined as filament surface heating, where a modified print nozzle is used to heat only the fiber surface while the fiber core is kept to a low temperature. The basis of filament surface heating is to allow the fiber cladding to adhere to adjacent deposited fibers through interdiffused polymeric chains, while the fiber core, which contains the active device structure, remains undeformed and functional. By fabricating fibers of different functionalities, a whole set of 3D devices, which can be customized both in its shape and functionality, can be constructed. For instance, the authors demonstrated the printing of a pixelated light-emitting 3D display, a photodetecting vase, and an omnidirectionally light-detecting sphere which spatially and locally detects light. By combining both light-emitting and light-detecting printed fibers, this work then describes the printing of an aeroplane wing which is able to interrogate miniscule structural defects at any point within the macroscale volume of the wing. Since there is a wide range of different fiber functionalities as published in previous works, this work sets a foundation toward future 3D printed structures that can be embedded with a large spectrum of multifunctionalities in them and can be shape-customized to different application needs.

## 4. Fiber Electronics for Biomedical and Healthcare Applications

Fibers, being 1D in form factor, are intrinsically flexible, making them mechanically suitable for a range of biomedical and healthcare applications. Specifically, functional electronic fibers have been harnessed as probes for optogenetics, conformal fabric for physiological sensing, and scaffolds for neuronal growth. In this section, we describe the materials characteristics and device performance of current multifunctional fibers in regards to the healthcare and biomedical fields. We also focus on their limitations, areas for improvement, and emerging functionalities.

### 4.1. Multifunctional Fiber Neural Probes

The emergence of optogenetics<sup>[101]</sup> has increased the use of optical fibers<sup>[102]</sup> in neuroscience as neural probes by which incident light is transmitted in and emitted light is guided back from the nervous system. Typical optical fibers are made up of high  $T_g$ , glassy materials that exhibit high moduli in the range of GPa. However, for biological applications, these properties

tend to evoke a foreign body immune response and cause glial scars at the interface between the fibers and tissues. To overcome these limitations, polymeric-based claddings in thermally drawn multimaterial fibers were first used by Canales et al.<sup>[103]</sup> to reduce the mechanical mismatch between the implanted fibers and tissue (Figure 7a–c). The nature of the polymeric cladding results in the fiber devices that possess low bending stiffness and achieve high endurance to repetitive deformation that takes place during tissue motion linked with respiration, heartbeat, and bodily locomotion. In their work, the fabricated multimaterial fiber was multimodal, enabling different forms of neuronal stimulations such as electrical impulses through conductive electrodes, optical stimulation via waveguides, and chemical infusion via microfluidic channels. These functional materials were fully integrated within a sub-millimeter fiber. Conductive materials, including carbon-loaded polyethylene or nontoxic low melting point metals such as tin, were incorporated within the fiber due to their glass transition temperatures being comparable to those of the polymers such as polycarbonate and cyclic olefin co-polymer (COC). They also highlighted the fiber's endurance to mechanical bending, evident by the minimal losses in electrical impedance and optical transmission (Figure 7d,e). Furthermore, electrical signals from the brain were still present up to two months from the in vivo implantation of the multifunctional fiber into a mouse's brain (Figure 7f). This showed that the multifunctional polymeric fiber is highly biocompatible and mechanically suited for interfacing the soft neural tissues of the brain.

One key challenge in the field of neural probes is increasing the biocompatibility of the multimodal fiber platform for long-term electrophysiological recording, while ensuring a high electrical conductivity for a good signal-to-noise ratio. Toward this aim, Park et al.<sup>[104]</sup> fabricated a thermally drawn, all-polymer fiber probe with polymer-based electrodes (Figure 7g,h) that were composite with graphite. These electrodes possessed electrical conductivity four times higher than that of the typically used carbon-based polyethylene electrodes, while the fiber maintained a low bending stiffness due to its fully polymeric characteristics. Its long-term capability and minimal trigger of foreign response was demonstrated by recording action potentials within the brain of a moving mouse (Figure 7i) up to 12 weeks upon implantation. The fiber also exhibited reduced glial scarring (Figure 7j–l) when compared to a thinner stainless steel microwire.

Beyond the studies of the neurons in the brain, Lu et al.<sup>[105]</sup> advanced the work of multifunctional fiber probes to investigate and interrogate neuronal circuits within the spinal cord. In order to withstand the repeated strains from the motion of the spinal cord and to match the low elastic modulus of the surrounding neural tissue, highly flexible stretchable probes were fabricated using the thermal drawing process. In their work, an optical fiber constituting of a polycarbonate core and a cyclic olefin co-polymer cladding was first thermally drawn. This fiber was later dip coated with a percolation of silver (Ag) nanowires and finally capped with a poly(dimethylsiloxane) (PDMS) coating (Figure 8a,b). Its flexible characteristics were demonstrated as light transmission through the optical fiber was sustained even under a bending curvature radius of 0.5 mm. In addition, as the fiber was stretched to twice its original length, the electrical conductivity of the fiber reduced by a relatively small factor of  $\approx 1.5$  (Figure 8c), highlighting

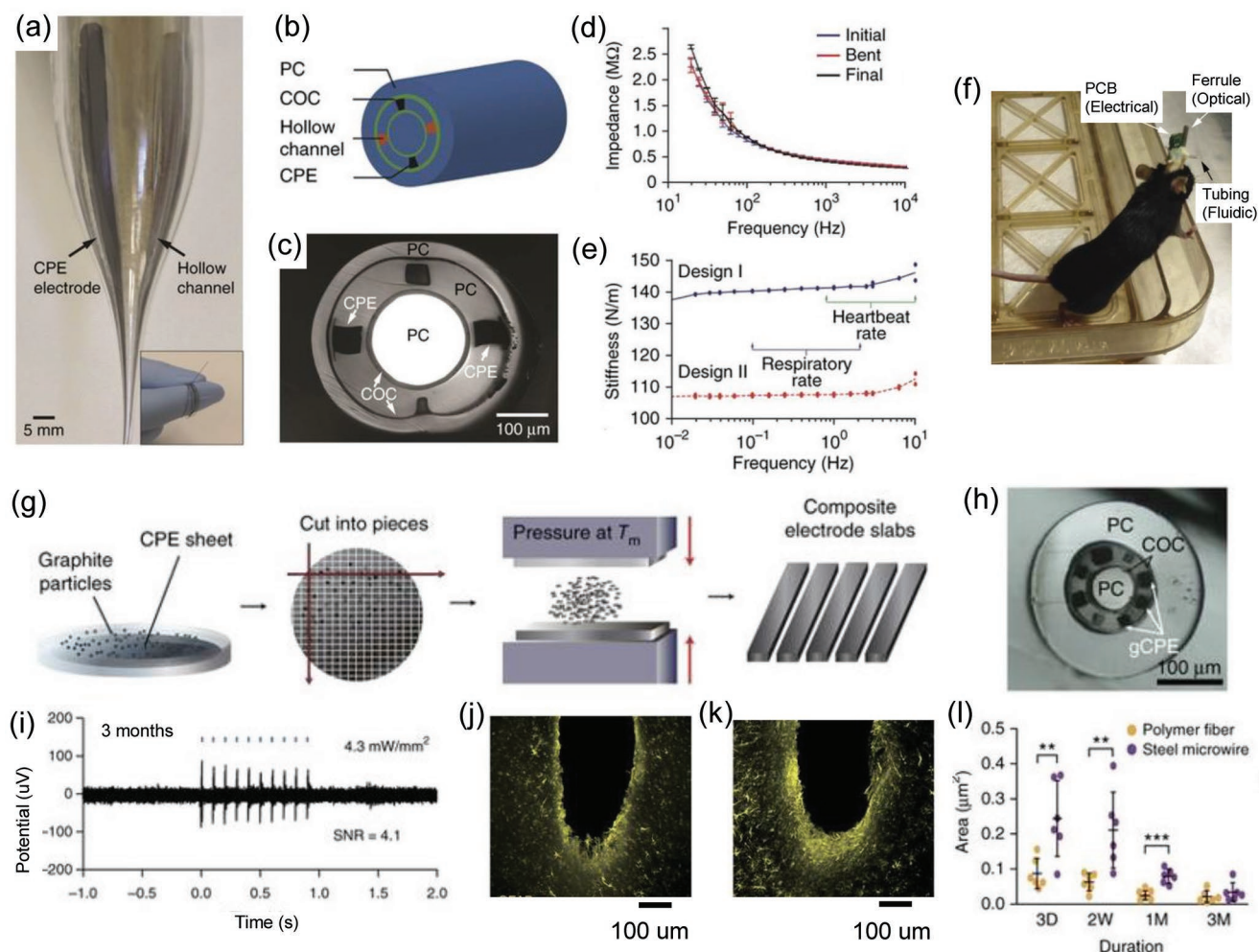


**Figure 7.** a) Photograph of the multimaterial preform with its necking into a multifunctional fiber probe. Inset shows the flexible fiber wrapped around a finger. b) Schematic and c) actual optical image of the fiber probe cross-section that shows multiple functionalities including electrodes (conducting polyethylene, CPE), waveguide (polycarbonate, PC, core), and hollow channels for microfluidics. d) Electrical impedance spectroscopy plot indicating that the fiber impedance remains unchanged as it is bent and recovered (final). e) Bending stiffness plots show little change in stiffness for varying mammal activities including respiration and heartbeat. f) Implantation of the multimodal fiber probe into a mouse's brain. a–f) Reproduced with permission.<sup>[103]</sup> Copyright 2015, Springer Nature. g) Schematic showing fabrication process of graphite-CPE (gCPE) electrodes. h) Cross-sectional image of the drawn fiber, illustrating the construction of multiple modality including PC waveguide core, gCPE electrodes and hollow channels. i) Electrophysiological recording of optically evoked potentials in the mice transfected with performed 3 months after implantation. j, k) Confocal images of glial scarring (green fluorescence) from 200  $\mu\text{m}$  fiber probe (j) and 125  $\mu\text{m}$  stainless steel microwire (k). l) Average fluorescence intensity comparing area of glial scarring between polymer fiber and steel microwire. g–l) Reproduced with permission.<sup>[104]</sup> Copyright 2017, Springer Nature.

its utility as a stretchable conductive fiber. Upon implantation of these fibers into the spinal cord of a mouse (Figure 8d), the neural activity, sensory-evoked (Figure 8e) and optically evoked potentials (Figure 8f), could be recorded by the conductive Ag nanowire mesh, in addition to the optical control of the hindlimb muscles. Further findings showed neither tissue erosion nor cytotoxic effects at the interfaces of the fiber implants, thus elucidating the practicality of these fibers as spinal cord implants.

#### 4.1.1. Material Studies on Soft Polymers and Elastic Electrodes

The search for materials that possess low elastic moduli and suitable viscoelasticity for thermal drawing represents an important step toward the widespread use of fiber probes. Polymeric

materials used in thermal drawing are usually thermoplastic, while rubbery, low elastic moduli polymers are typically thermosets that are not suited for thermal drawing. As described in Section 3.4, SEBS, a thermoplastic elastomer, permits production of highly elastic fibers. These polymers contain both molecular cross-linkages for its elasticity and weak van der Waals bonding between polymeric chains that result in its thermoplasticity. It would be valuable for future works to investigate the long-lasting performance of these thermally drawn elastic fibers for in vivo implantation. In addition, while the mechanical properties of flexible, stretchable probes are well demonstrated, the functionality of the probe, such as its electrical conductivity, is nevertheless still compromised at higher strain levels due to breakages in the conductive percolation network. New materials or mechanisms that allow conductive electrodes to be stretched or bent



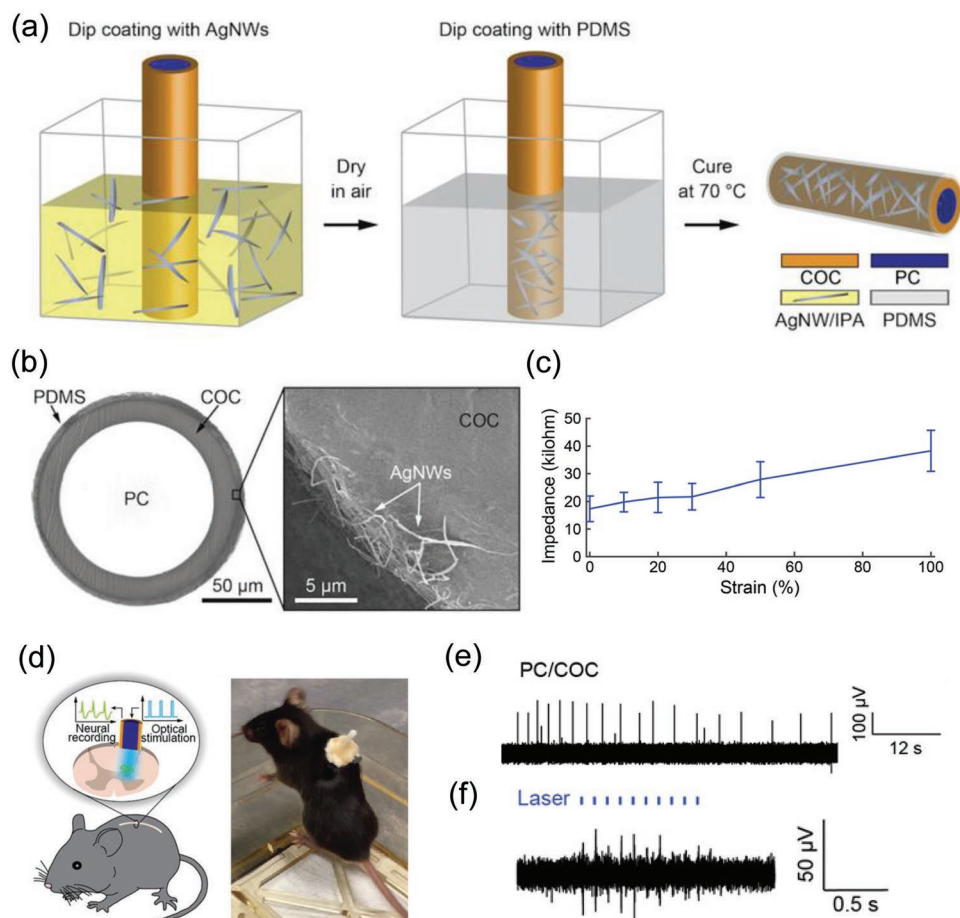


**Figure 8.** a) Fabrication process of a flexible stretchable multimodal fiber probe. b) Cross-sectional optical image illustrating the PC/COC waveguide and a PDMS overlayer. Between them is a mesh of conductive silver nanowires, AgNWs, mesh (SEM image on the right). c) Electrical impedance of the AgNWs mesh increases as the fiber is stretched. d) Schematic (left) and photograph (right) of the implantation of the fiber probe into the spinal cord of a mouse. e) Sensory-evoked and f) optically evoked action potential measured by the AgNWs mesh. Light traverse through the PC core for the measurement of the optically evoked potential. a–f) Reproduced with permission.<sup>[105]</sup> Copyright 2017, The Authors, published by American Association for the Advancement of Science (AAAS). Reprinted/adapted from ref. [105]. © The Authors, some rights reserved; exclusive licensee American Association for the Advancement of Science. Distributed under a Creative Commons Attribution NonCommercial License 4.0 (CC BY-NC) <http://creativecommons.org/licenses/by-nc/4.0/>.

without reducing their conductivities should be investigated. For example, one approach considered is the introduction of liquid metal, such as gallium or galinstan, into the channels of the fiber. As the elastic cladding is stretched, the encapsulated liquid metal can be deformed accordingly, hence retaining its conductive path. However, even if these metals are biocompatible, its liquid characteristics may cause uncontrolled release of metals into the tissue. Another means of obtaining stretchable electrodes is by introducing structural elasticity, by using conductive helices<sup>[106,107]</sup> or buckled electrodes<sup>[108,109]</sup> within or around the fiber for example. High melting point ( $T_m$ ) metals such as tungsten have low electrical impedance but exhibit high elastic moduli, which are undesired for tissue implantation. On the other hand, conductive polymeric composites such as carbon-loaded polyethylene have low elastic moduli but exhibit high electrical impedance, resulting in poor signal to noise ratio. As such, the introduction of structural elasticity to high  $T_m$  metals can offer the best of both mechanical and electrical characteristics: low elastic moduli and low impedance.

#### 4.1.2. Other Emerging Probe Functionalities

Other than their use as neural probes, thermally drawn fibers have also been commercialized as flexible probe-like surgical tools in removing tumors from the body via laser ablation. Based on the technology of the dielectric mirror, Temelkuran et al.<sup>[26]</sup> fabricated a hollow core photonic crystal fiber with arsenic selenide ( $\text{As}_2\text{Se}_3$ )—PES multilayers (Figure 9a,b) of alternating refractive indices with sub-micrometer thicknesses. In addition to the complexity of how different material classes (polymer and semiconducting glass) can be interfaced together, this work also illustrates the ability of thermal drawing to achieve nanoscale features. These multilayers exhibit a photonic bandgap in wavelengths relevant to that of the  $\text{CO}_2$  laser, enabling light of wavelengths (0.75–10.6 μm) to transmit across tens of meters of fiber and multiple bends with transmission losses of less than 1.0 dB  $\text{m}^{-1}$  (Figure 9c). Coupled with the manufacturability of the thermal drawing technique, these optical advantages facilitate the realization of these fibers for real-world medical applications.

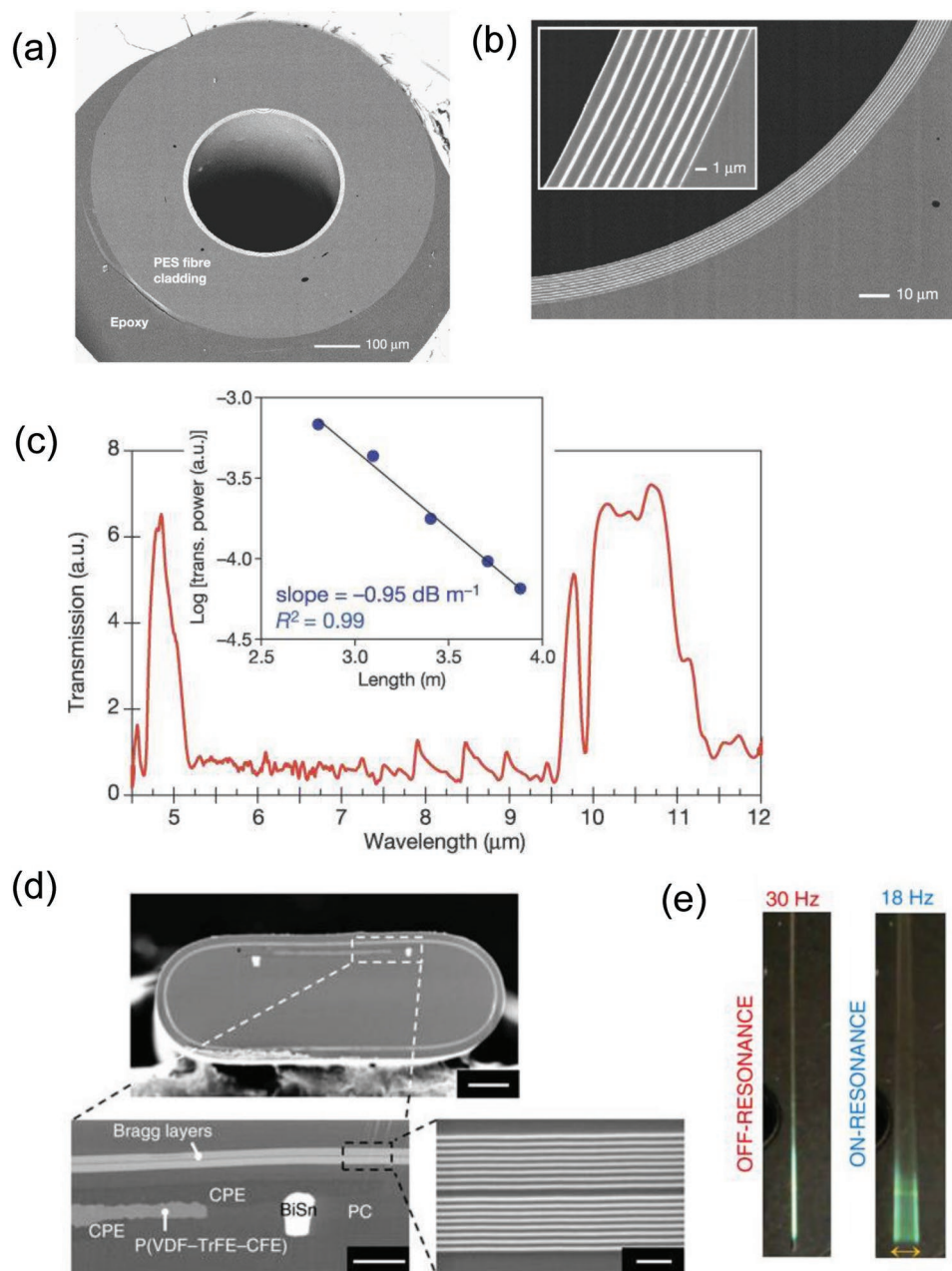


**Figure 9.** a,b) SEM cross-sectional images of: a) the thermally drawn photonic bandgap fiber containing a PES cladding and a hollow core surrounded by b) a multilayered structure of  $\text{As}_2\text{S}_3$  layers (bright white) and PES layers (gray). c) Transmission spectrum of light traversing through the hollow core indicating low loss of  $0.95 \text{ dB m}^{-1}$ . a–c) Reproduced with permission.<sup>[26]</sup> Copyright 2002, Springer Nature. d) SEM cross-sectional image of the electrostrictive microelectromechanical (MEM) fiber illustrating the piezoelectric P(VDF-TrFE-CFE) layer interfaced by the CPE electrodes. BiSn electrodes are electrically connected to the CPE for higher conductivity along the fiber length. A shell of multilayer  $\text{As}_2\text{S}_3/\text{PC}$  structure surrounds the fiber to attain optical Bragg reflection for fiber deflection characterization. Scale bars for top, bottom left, and bottom right are 100, 20, and 2  $\mu\text{m}$ , respectively. e) Mechanical actuation of the MEM fiber at OFF- and ON-resonance states. d,e) Reproduced under the terms of the CC-BY Creative Commons Attribution 4.0 International License (<http://creativecommons.org/licenses/by/4.0/>).<sup>[23]</sup> Copyright 2017, The Authors, published by Springer Nature.

There are also many other forms of stimulation that have yet to be explored from fiber neural probes. For example, other than neuronal probing via optical, electrical, and chemical means, electrostrictive P(VDF-TrFE-CFE) micro-electro-mechanical fibers<sup>[23]</sup> (Figure 9d) can be used to transmit mechanical actuating stimuli (Figure 9e) to the neurons<sup>[110,111]</sup> or detect changes in the strain environment of surrounding tissues.<sup>[112,113]</sup>

In addition, neuronal stimulation currently is limited to the fiber tip. It would be interesting to explore multiple surface-exposed stimulation and interrogation sites along the length of the fiber. Doing so would permit the investigation of the distribution and properties of neurons in the brain or the spinal cord with both spatial and temporal resolution. Thermally drawn fibers are translationally symmetric, meaning their cross-sectional material

structures are similar continuously along their lengths. This impedes spatial discrimination of sensing signals at different fiber positions. A preliminary step toward spatial sensing is in breaking the fiber translational symmetry, which is discussed briefly in the previous section for high-temperature materials. For materials with lower melting points, Kaufman and colleagues<sup>[29]</sup> exploited Rayleigh capillary instability to break the continuous fiber structure into discrete sphere-like structures (Figure 10a). The transformation of cylindrical rods into spheres was attributed to the inclination toward the lowest surface energy state of a sphere.

This work demonstrated the capillary breakup of in-fiber structure across different materials including a polymeric COC core in polycarbonate and a semiconducting chalcogenide glass ( $\text{As}_2\text{Se}_3$ ) core in polyethersulfone (PES). It also demonstrated the in-fiber structure tunability across a range of sizes, from nano to micro-scale (Figure 10b).

Further work by Rein et al.<sup>[34]</sup> described selective breakup of different materials, in which both 1D and 0D structures are present in the thermally drawn fiber. To achieve this, the dependence of the breakup time-scale on the feature size was used. More specifically, the transformation time increases with larger feature size. Hence, by tailoring the sizes of different materials within the fiber, the material with a smaller width breaks up faster than that of a bigger dimension. This work further expanded the possible in-fiber architectures by interconnecting broken-up semiconducting spheres with continuous conductive electrodes (Figure 10c–f). Furthermore, illuminating spheres with a laser beam generates Mie optical resonance in these spheres. The resonant effects could be quantified through measurements from the photodetecting spheres, which are read out at the ends of the fiber. It is envisioned that fibers with such multiplicity of discrete spheres and continuous electrodes be implemented as neural probes of spatial functionalities.

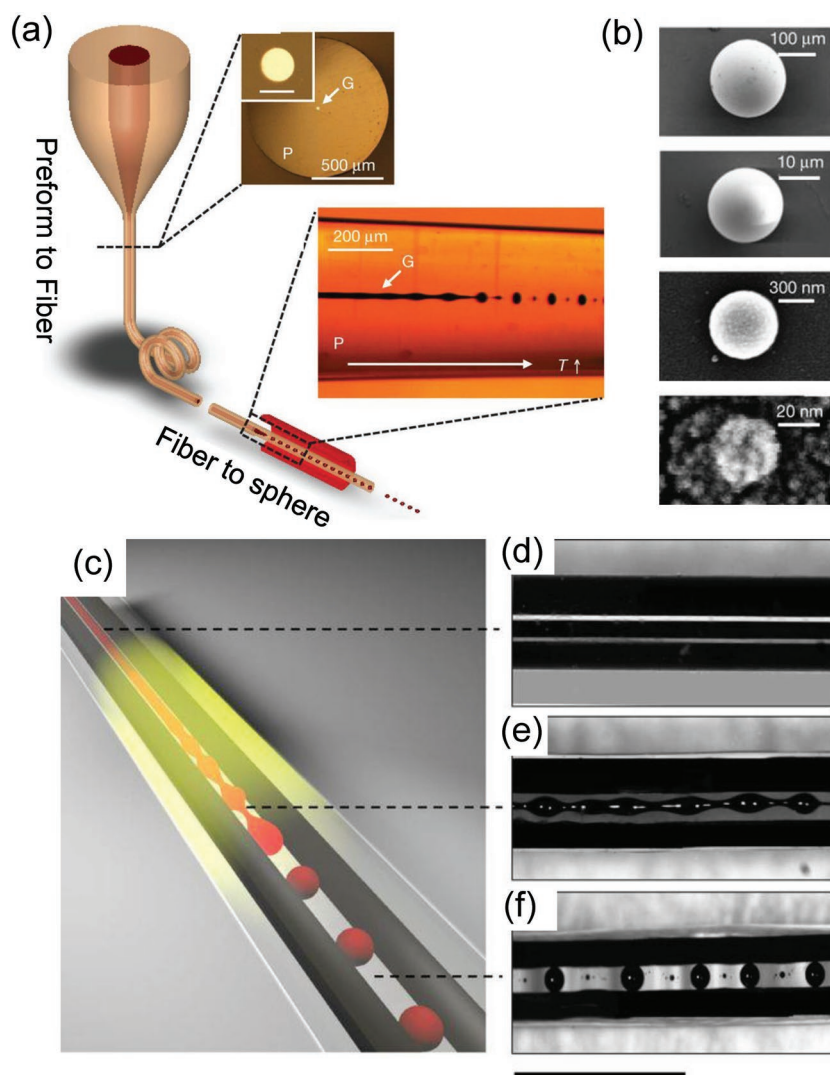


**Figure 10.** a) Fabrication scheme to generate in-fiber spheres. A fiber with an  $\text{As}_2\text{Se}_3$  glass core (G) encased in a PES polymer cladding (P) is thermally drawn and later fed into a heated furnace. The inset shows the glassy core becoming unstable and transforming into spheres due to capillary instability at higher temperature. b) Size-tunable spheres formation from nano- to microscale. a,b) Reproduced with permission.<sup>[29]</sup> Copyright 2012, Springer Nature. c) Schematic of selective capillary breakup of different materials enabling 0D discrete chalcogenide glass to be flanked by 1D continuous electrodes in the fiber. d–f) Optical images of the fiber: d) at the onset, showing continuous structure for the two materials, e) at an intermediate time, showing the transition into spheres, and f) after breakup, showing discrete chalcogenide spheres electrically connected to the adjacent electrodes. Scale bar is 1 mm. c–f) Reproduced under the terms of the CC-BY Creative Commons Attribution 4.0 International License (<http://creativecommons.org/licenses/by/4.0/>).<sup>[34]</sup> Copyright 2016, The Authors, published by Springer Nature.

## 4.2. Fibers as Regenerative Neuronal Scaffolds

The recovery of injured neural tissue is slow especially for tissue with damage exceeding 3 cm in length, which results in life-long disabilities<sup>[114–116]</sup> for approximately half of those who suffer from extensive nerve damage. Implanting a scaffold at the injured region can support the regenerative growth of neural tissue.<sup>[117,118]</sup> Thus far, neuronal growth can be guided and accelerated by several factors: topography,<sup>[119–121]</sup> chemical gradients,<sup>[122,123]</sup> or stimulus of growth via optogenetics.<sup>[124]</sup> The thermal-drawing process offers advantages in fabricating structurally designable fiber scaffolds of different materials, shapes, and functionalities to support these guided growths. For topography-guided growth, Koppes et al.<sup>[125]</sup> fabricated polyetherimide (PEI) fiber scaffolds with cylindrical, rectangular, and grooved channels (Figure 11a). The size of the channels is tuned by controlling the stresses imposed during thermal-drawing. It was found that neuronal growth along the length of the fiber scaffold (Figure 11b,c) is enhanced in rectangular channels compared to circular channels. In addition, introducing micro-grooves onto the surface of the channel walls



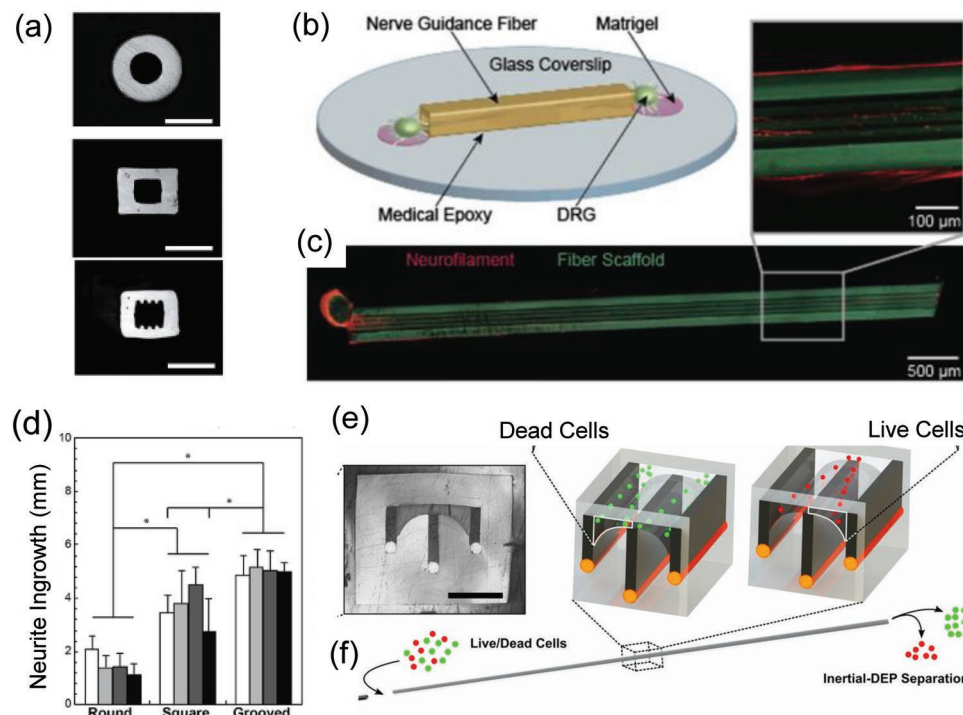


**Figure 11.** a) Optical cross-sectional images of neural guidance fiber with (top) circular, (middle) square and (bottom) grooved channels. Scale bars = 200  $\mu$ m. b) Schematic of the DRG-seeded fiber. c) Optical image showing the neurite ingrowth through a 5 mm, grooved fiber scaffold. The inset shows a higher magnification image of neurite orientation along the grooves. d) Average ingrowth distance after 14 days for round, square, and grooved channels. The scaffolds are seeded at one end. Longer growth is observed for the grooved channels. a–d) Reproduced with permission.<sup>[125]</sup> Copyright 2016, Elsevier. e) Cross-sectional optical of a microfluidic fiber containing an arbitrarily shaped microchannel with surrounding CPE electrodes (black). Scale bar, 200  $\mu$ m. f) Schematic of flowing live and dead cells through the fiber. The different cell types are subjected to different magnitudes of inertial and dielectrophoretic (DEP) forces, resulting in particle movement to different positions within the fiber. e,f) Reproduced with permission.<sup>[130]</sup> Copyright 2018, National Academy of Sciences.

enables neurite alignment and thus higher directional growth along the fiber (Figure 11d). This finding is further supported by the works of Nguyen-Dang et al.,<sup>[126]</sup> in which the growth of dorsal root ganglia (DRG) occurs more preferentially and orderly along the textured surfaces of a PDMS fiber as opposed to the random growth on a nontextured surface.

In addition, optical and electrical simulations accelerate neuronal growth. For instance, delivering pulsed blue light<sup>[124]</sup> enhances neurites outgrowth from peripheral neural tissue of DRGs expressing channelrhodopsin 2 (ChR2), while applying a DC or AC electric field<sup>[127,128]</sup> enhances neurite sprouting and growth as well as Schwann cell proliferation.<sup>[129]</sup> Hence, the integration of light-emitters or optical waveguides into fiber scaffolds will be useful in creating multifunctional scaffolds for regenerative neuron growth. However, thermally drawn fiber scaffolds that house all functional units including the channel for neuronal growth, electrodes, and waveguides have not yet been demonstrated. Nevertheless, a preliminary preview of such a fiber is demonstrated by Yuan et al.<sup>[130]</sup> They fabricated thermally drawn microfluidic fibers that are integrated with electrodes positioned around a microchannel (Figure 11e). The flow of particles and cells through the optimally shaped microchannels is controlled and directed by electric fields applied across the electrodes within the fiber so as to separate living and dead cells (Figure 11f). While this fiber is not directly implemented as a scaffold, it is indicative of current complex

fiber architectures that can enable future electronics-integrated scaffolds for highly regenerative neuronal growth.

#### 4.2.1. Combining Porosity and Microchannels

The works reported above describe fiber scaffolds with microchannels that are fully enclosed except at the ends of the fiber. However, accelerating neuronal growth requires the exchange of nutrients such as oxygen. Thus, the fiber scaffold must be open to the external environment, yet still contain a confined microchannel for directed growth. One solution for open fiber scaffolds is introducing porosity in the fiber cladding. This is demonstrated by Grena et al.,<sup>[131]</sup> who achieved porosity in fibers in situ during the thermal drawing process by implementing thermally induced phase segregation (TIPS) of a polymer–solvent mixture. From this process, porous fibers of varying materials, including biodegradable polycaprolactone (PCL) and polyvinylidene fluoride (PVDF), and different shapes were produced. In addition, by controlling the quenching temperature, pore sizes ranging from 500 nm to 10  $\mu$ m were achieved. Taking porous fibers a step further, recent work by Shahriri et al.<sup>[132]</sup> introduces PCL porous fibers with microchannels. This work presents an alternative method to create porosity in fibers by salt leaching. Salt crystals and PCL are mixed, molded into a preform, and later

drawn into a fiber, before soaking in a solvent to remove the salt particles leaving behind a porous fiber. Varying the sizes and the amount of the salt changes the pore size and porosity volume. Finally, for its application as a nerve scaffold, this work demonstrates the printing of these porous fibers into centimeter-scale scaffolds with shapes that tailor to the exact dimensions and structures of the nerve gap within the spinal cord or in bifurcated nerves. These printed scaffolds contain tens of microchannels, surrounded by porous walls for nutrients exchange toward fast neurite growth.

### 4.3. Physiological Sensing from Functional Fabrics

In addition to the *in vivo* implementation of these fibers as probes and scaffolds, electronic fibers can be used as a non-invasive flexible platform that make direct conformal contact with bodily skin to sense physiological parameters. Given the substantial interaction area between clothing and the body, the ability to interrogate physiological signals via fibers and fabrics could be useful in diagnosing, tracking, and investigating health conditions.<sup>[133–135]</sup> In this subsection, we discuss the current functional capabilities of multimaterial fibers for the purpose of physiological sensing.

#### 4.3.1. Thermal-Sensing Fibers

Our body temperature is indicative of a number of possible physiological conditions,<sup>[136–140]</sup> including sepsis, infection, shock, and even anxiety. Fibers with the ability to measure body core temperature can thus be beneficial in preventing and tracking these conditions. However, precisely monitoring and detecting thermal excitation over a large area with highly curved geometrical features still remains technologically challenging. Bayindir et al.<sup>[20]</sup> developed a thermal sensing fiber that is comprised of a temperature-sensitive multicomponent semiconductor ( $\text{Ge}_{17}\text{As}_{23}\text{Se}_{14}\text{Te}_{46}$ ) interfaced with four metallic electrodes. The mechanism through which this device detects thermal changes is the thermoresistive effect, which correlates the change in electrical resistance across electrodes to the absolute temperature of the semiconductor via an exponential relation. The composition of the semiconductor was chosen such that the electronic mobility gap of the material is small and electrical responsivity is high upon small temperature changes. Heating a single fiber above or cooling below the room temperature showed that the temporal response of the fiber is in the range of several seconds. This work further demonstrated the capability of localizing the temperature distribution over a large area using a crosshatched fiber-mesh with 1 cm separation distance between neighboring fibers. Its mechanical flexibility was highlighted by conformally wrapping the fiber-mesh around a mannequin head. A thermal map could be reconstructed using signals obtained by connecting each fiber to external circuits. The dynamical thermal map obtained by the fiber array was in good agreement with the data acquired by an infrared camera. This thermal sensing fiber mesh was also able to pinpoint the spatial location and heat distribution of a contacting heat source.

#### 4.3.2. Diode Fibers Enabling Heartbeat Sensing

The rate and variabilities of blood pulsation reveal the status of the cardiovascular system.<sup>[141,142]</sup> Commercial heartbeat sensors utilize both light-emitting and photodetecting diodes that exhibit high optoelectronic performance to enable high sensing sensitivity. Toward this aim, Rein et al.<sup>[35]</sup> introduced a new thermal-drawing approach to establish connections to commercial microscale diode devices within the fibers. This work combines the scalability of the thermal-draw process in forming long-length fibers with pre-made commercial devices (Figure 12a). Specifically, discrete devices are first embedded into the preform without any connections. During the draw itself, electrical wires are also fed into the milled channels within the preform. As the preform is scaled down into a smaller sized fiber, the wires are brought closer together until they eventually contact the devices (Figure 12b). Doing so allows hundreds of devices to make electrical contacts within the fiber in a single draw. Finally, with electrical connections made to the discrete optoelectronic devices, they are shown to emit light of varying wavelengths (red, green, and blue) (Figure 12c) and detect at a high bandwidth and sensitivity which is orders of magnitude larger than of previous thermally drawn optoelectronic fibers. Later, green light-emitting and light-detecting fibers are woven side by side within a single fabric (Figure 12d). They combine to form an optical pulsation sensor via photoplethysmography. As red blood cells absorb green emitted light, the light intensity sensed by the light-detecting fiber varies correspondingly with the in-and-out amount of red blood cells, thus enabling readout on the heartbeat (Figure 12e). As a future step, since hemoglobin in red blood cells absorbs more red light at higher oxygen level, while deoxygenated hemoglobin absorbs more infrared light, a set of red and near infrared light emitting fibers, accompanied by the light detecting fiber, can potentially operate as an oximeter.<sup>[143–145]</sup>

#### 4.3.3. Other Forms of Physiological Sensing

There is still a multitude of useful physiological data that has yet to be collected and utilized from the interfaces of electronic fibers and the human body. For instance, skin excretes sweat that contains many useful chemical markers<sup>[146,147]</sup> such as glucose level, blood lactate, and uric acid. A fabric with a distributed, wide-area, sweat-sensing capability can potentially provide quick, accurate, and large-scale analysis of the sweat markers. Chemical-sensing fibers, in particular Gumennik et al.<sup>[21]</sup> and Stolyokov et al.,<sup>[85]</sup> which are introduced in the previous section, are an important step toward sweat sensing. These studies describe the different possible fiber device configurations that facilitate electrical or optical readout of chemicals, which may include sweat-sensing agents. While these chemical-sensing fibers demonstrate a viable approach for achieving sweat-sensing fibers, there are still limitations that reduce their utility. For instance, the fibers in both works are fully cladded by a thermoplastic polymer, resulting in chemical sensing occurring either at the tip of the fiber or along a fiber surface that must be manually cleaved, as the presence of cladding impedes sensing across the full length of the fiber. In addition, the incorporation

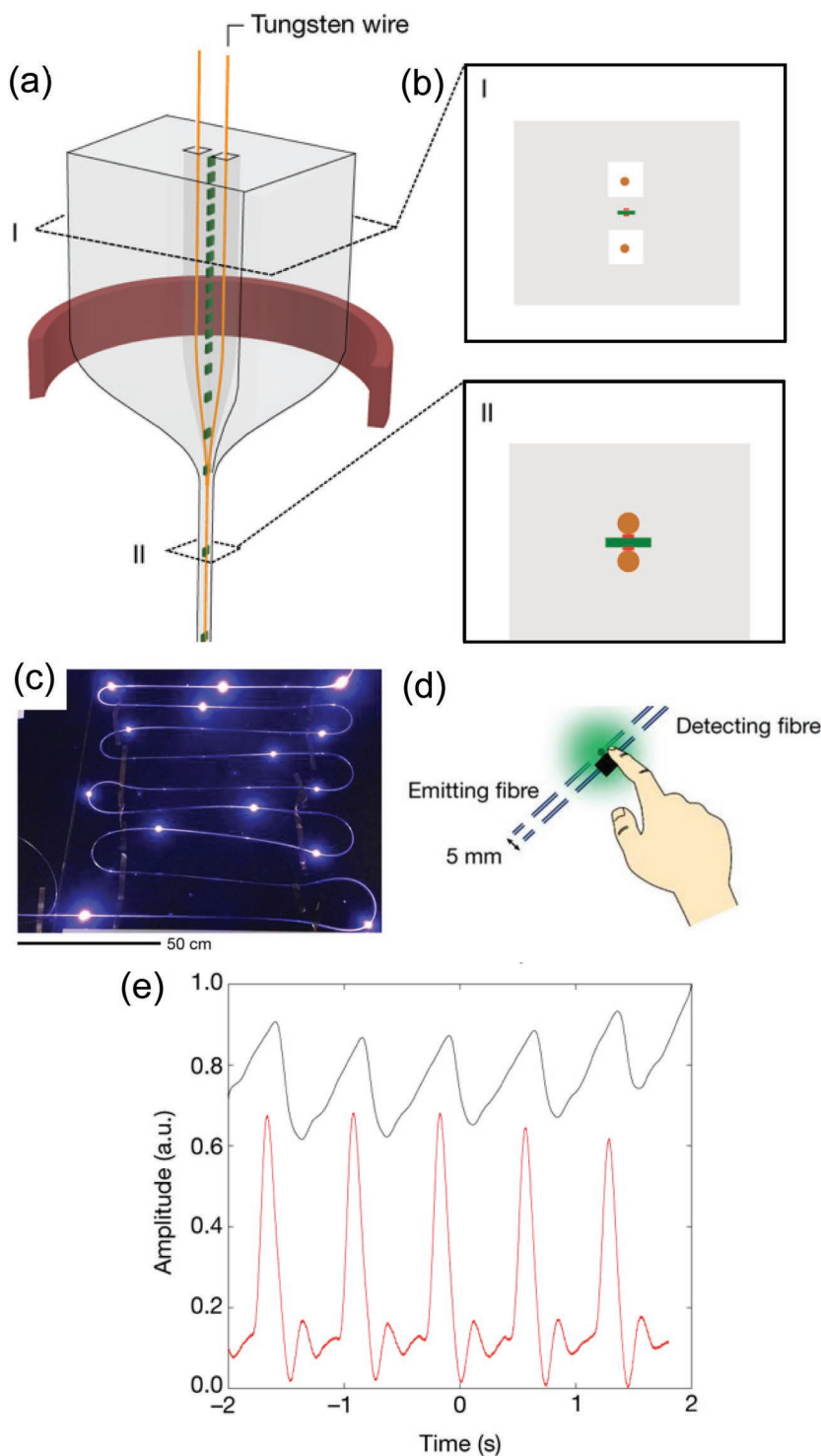


**Figure 12.** a) Schematic of the thermal draw process with devices embedded and wires fed into the preform. b) In the preform stage, the wires and devices are spaced far apart (I). As the preform necks into a fiber, the wires are brought closer together until they contact the devices (II). c) Photograph of blue-light-emitting diode fibers via thermal drawing of embedded devices. d) Schematic of a finger touching a light-emitting and light-detecting fibers that are woven in a fabric. e) By touching on these fibers, the measured reflected light amplitude gives the heartrate. The top black curve in the plot is the experimental data, while the bottom red curve is measured by a commercial sensor. The periodic amplitude corresponds to the frequency of the blood pulsation. a–e) Reproduced with permission.<sup>[35]</sup> Copyright 2018, Springer Nature.

of the sensing agents into the fiber is performed post-draw, thus reducing its fabrication scalability. The improvements necessary for the practicality and scalability of a sweat-sensing fiber have to be made on the following fronts: i) surface-exposed sensing agents that are stable in the presence potential moisture or mechanical degradation, ii) efficient conversion of chemical to electrical/optical signals, and iii) sensitive readout of these signals across the length of the fiber, which may be on the meter scale. The next step toward sweat-sensing fibers is identifying suitable materials or composites that are made up of the relevant, stable, chemical-sensing agents, while being thermally drawable. In addition, good interfacial electrical connections between the sensing agents and electrodes will be key to efficient and sensitive sensing performance.

## 5. Energy Harvesting and Storage Fibers

The human body represents roughly two square meters of dynamic and ever-moving surfaces—most of which are covered by some form of fabric. The opportunity to utilize this large area for energy harvesting and storage has been explored for the last few decades. Since the material categories of thermally drawn fibers exhibit a number of functionalities compatible with energy generation and storage, studying these fibers becomes exciting especially for building textile-compatible, self-powered, integrated systems. Indeed, there exists an abundance of energy sources that are sustainable, free, safe, clean, and importantly, as compared to fossil and nuclear energy sources, scalable into powering of mobile devices. In daily life, the human body is continuously exchanging different forms of energy. Furthermore, electromagnetic solar radiation incident on the human body is absorbed by cellular organisms to power vital functionalities. These and other energy sources in and around the human body motivate researchers to develop self-powered systems that avoid the size and weight burden of external power supplies.

Previous efforts to produce portable energy generation and storage systems that take advantage of these natural energy sources resulted in bulky, unsafe, and inconvenient to wear systems. Therefore they have not been widely adopted by consumers.<sup>[148]</sup> In contrast, the thermal drawing approach is advantageous in its fully packaged, flexible,



and lightweight in-fiber devices, which enable fiber-woven fabrics to provide power needs without additional size or weight from external connection. This section reviews the capability of fibers to harvest and store energy.

### 5.1. Energy Storage Fibers

The fiber geometry is suitable for power storage using fiber battery or supercapacitors. Fiber-based energy storage is important to power integrated fiber devices. There have been a number of efforts focused on the fabrication of electrochemical energy storage fibers. Great academic progress has been made through the discovery of new high-performance active fiber materials such as carbon nanotubes (CNT), reduced graphene oxide (rGO)/CNT,  $\text{MnO}_2$ , and conducting polymers on centimeter scale fibers. The fabrication of electrochemical fibers can be categorized in two distinct routes: 1) solid-state processes wherein carbon nanotubes are directly spun into a fiber from the synthesis reaction zone<sup>[149,150]</sup> or a CNT forest during spinning,<sup>[151]</sup> or 2) wet processes wherein carbon nanomaterials are dispersed in a fluid, extruded out, and coagulated into a solid fiber.<sup>[152]</sup> Fabricating supercapacitor and battery fibers requires a multistep process, involving not only nanomaterial integration but also electrolyte coating and small-scale multifilament assembly. These approaches result in intra- and interfiber defects that, in turn, directly affect the electrical and ionic conductivity of the fiber devices. The key enablers of fiber-shaped energy storage devices are the length, which needs to be comparable with traditional textile fibers for machine weavability, and the energy density, which should be approximately equivalent to conventional energy storage systems; however, no system has been able to achieve this goal yet.

Typically, preforms are composed of thermoplastic or glass materials with thermomechanical properties that are compatible with the preform-to-fiber thermal drawing process. However, active materials typically used in energy storage systems are not intrinsically compatible with this process. For example, electrolytes commonly used in batteries are liquid-based, which results in lumps in the fiber during thermal drawing, thus impeding co-drawability with other materials such as the electrodes. In addition, thermal drawing is typically performed in an open environment exposed to air, but moisture-sensitive energy storage materials may degrade upon exposure to air. Thus, there exists a need to design new active materials that can leverage the thermal draw process in order to produce fibers with outstanding energy storage properties at scale.

There have been previous efforts to draw electrostatic fiber capacitors with interdigitated electrodes.<sup>[153]</sup> Capacitors are well known to store charges across electrodes that are separated by a dielectric. In this work, PVDF material was utilized as a dielectric medium. To enhance the capacitance, the contacting surface area between dielectric and electrodes can be increased by folding it into several layers (Figure 13a,b). Figure 13c shows that as the number of layers increases from one to six folds, the capacitance for a 50 cm fiber capacitor increases from 1 to 25 nF (Figure 13c). This work represents an early demonstration of in-fiber energy and charge storage. Further studies to

enhance its energy storage ability include infusing electrolyte solution as the active functional medium, rather than using a solid-state dielectric medium, so as to form fibers with supercapacitor capabilities.

### 5.2. Energy Harvesting Fibers

For energy harvesting, there are multiple suitable effects that can be operated from a fiber system. The piezoelectric effect converts stress or pressure into electricity. Triboelectricity takes advantage of the surface electrification effect between two different kinds of surfaces. Photovoltaics convert light into power. The thermoelectric (TE) effect exploits a temperature difference to generate electricity. These energy sources are sustainable, cheap, lightweight, and complementary to each other for continuous energy supply. In addition, the growing power needs of aerial and ground-based objects, such as drones and military wear, motivate a focused thrust on fiber and fabric energy solutions that are equipped with on-demand energy harvesting capabilities that are both highly efficient and lightweight. In this subsection, we will discuss the multimaterial fiber drawing phenomena as an enabling tool for energy harvesting.

#### 5.2.1. Photovoltaic Fibers

Using the thermal fiber drawing technique as a preliminary step to create a templated hollow silica fiber, He et al.<sup>[60]</sup> reported photovoltaic fibers based on silicon p–i–n photodiode junctions fabricated via subsequent HPCVD (Figure 13d,e). They demonstrate that silicon layers can be deposited over lengths of more than 10 m in fiber channels with the fiber exhibiting enough flexibility to be tied into tight knot (Figure 13f,g). To characterize the layer compositions radially across the fiber cross-section, the authors made use of Raman spectroscopy to correlate the value of the inverse of the Raman profile asymmetry ( $q^{-1}$ ) with the doping concentration. Plotting out  $q^{-1}$  against the radial distance shows the p-doped, intrinsic, and n-doped sections (Figure 13h). These p–i–n photodiode junction fibers function as optoelectronic devices for both solar-cell applications and high-speed (1.8 GHz) photodetectors (Figure 13i). To further improve the efficiency of photovoltaic conversion and light detection, advanced light-management schemes including controlling the fiber waveguide behavior was harnessed.

This work is a preliminary study aimed at introducing silicon-based junctions into fibers with thermal drawing. Further studies are still required to understand the fundamental kinetic and thermodynamic processes for reliably producing p–n junctions in fibers. By understanding the basic physics driving the PN junction formation in thermally drawn fibers, one could design and produce PV fibers, with high yield and efficiency and in a form factor that is compatible with weaving for upstream fabric integration, and finally create all-fiber PV solutions that surpass anything currently possible.<sup>[154,155]</sup> The ability to produce silicon microwires using a high-temperature fiber drawing system might facilitate the realization of this motivation.<sup>[39]</sup> This technique allows drawing of centimeter scale silicon rod into micro, even nanoscale, silicon wires inside of a

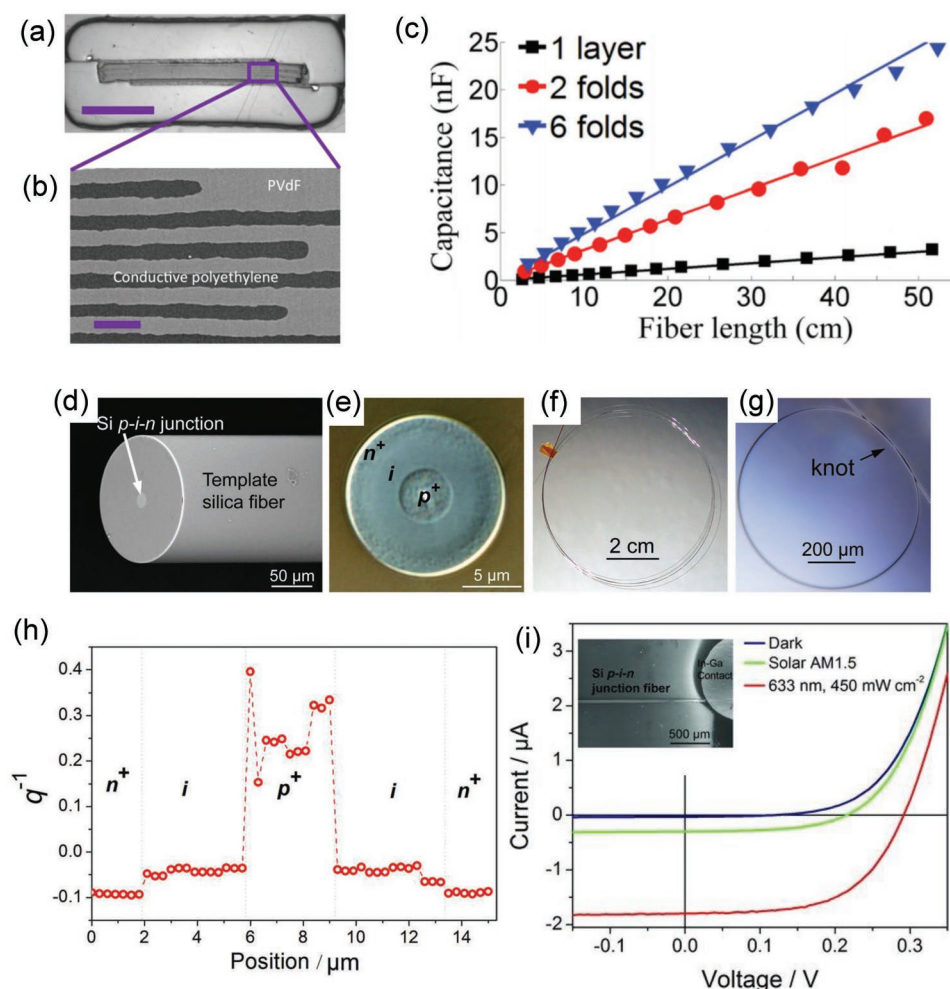


**Figure 13.** a) Optical micrograph of a fiber capacitor. Scale bar is 300 μm. b) SEM micrograph of the core region of the fiber, showing the interdigitated structure of the PVDF dielectric and the conductive polyethylene conductor. Scale bar is 20 μm. c) Capacitance of fibers measured as a function of length, for fibers with different numbers of PVDF/CPE folds. Increasing the number of folds enables to increase the capacitor surface area for a given length and thus increasing capacitance. a–c) Reproduced with permission.<sup>[153]</sup> Copyright 2013, AIP Publishing. Silicon p–i–n junction fibers fabricated in capillary templates via high-pressure chemical vapor deposition. d) SEM micrograph of a deposited and cleaved junction silicon p–i–n fiber fabricated in capillary templates via high-pressure chemical vapor deposition. e) Differential interference contrast (DIC) optical micrograph of a representative 15 μm diameter Si p–i–n junction. f) A junction fiber within a ≈ 1 m long silica template wrapped into a coil. g) A 6 μm diameter silicon junction-fiber core etched out of its silica cladding can be manipulated into a tight knot. h) Abrupt junction profile, obtained via Raman spectroscopy, representing the p–i–n compositions. i) Current–voltage profile of the Si junction fiber, illustrating its solar cell and photodetecting capabilities. Inset shows the In–Ga eutectic electrical connections made to the n- and p-doped layers. d–i) Reproduced with permission.<sup>[60]</sup> Copyright 2013, Wiley-VCH.

silica cladding. Further studies show that a self-developed p–n junction scheme can be created inside the fibers via the formation of capillary spheres through the Rayleigh–Plateau instability. However, a fully integrated PV fiber with all-continuous thermally drawn p–n junctions and electrodes remains unexplored. This requires forming distinct interconnects between the p–n junction systems to in-fiber electrodes, which is a technical challenge in high-temperature thermal drawing due to intermixing.

### 5.2.2. Thermoelectric Fibers

TE power generation<sup>[156,157]</sup> is another form of carrier-based energy harvesting in fiber form factor. TE fibers and fabrics

can be used not only to generate electricity from the natural temperature gradient present between the human body and the colder outside air temperature, but can also recover some of the dissipated heat generated by a PV cell integrated within the same fiber. To date, the TE effect has been investigated in a fiber platform by Zhang et al.<sup>[158]</sup> They fabricated crystalline thermoelectric micro/nanowires by thermally drawing hermetically sealed high-quality inorganic thermoelectric materials in a flexible fiber-like substrate (Figure 14a). The resulting thermoelectric fibers were intrinsically crystalline, highly flexible, ultra-long, and mechanically stable (Figure 14b,c), which enables them to be woven into a fabric (Figure 14d). This wearable 2D cooling textile was assembled to achieve a maximum cooling of 5 °C with an input current of 2 mA. These thermoelectric fibers were later used as energy generators by implementing them in

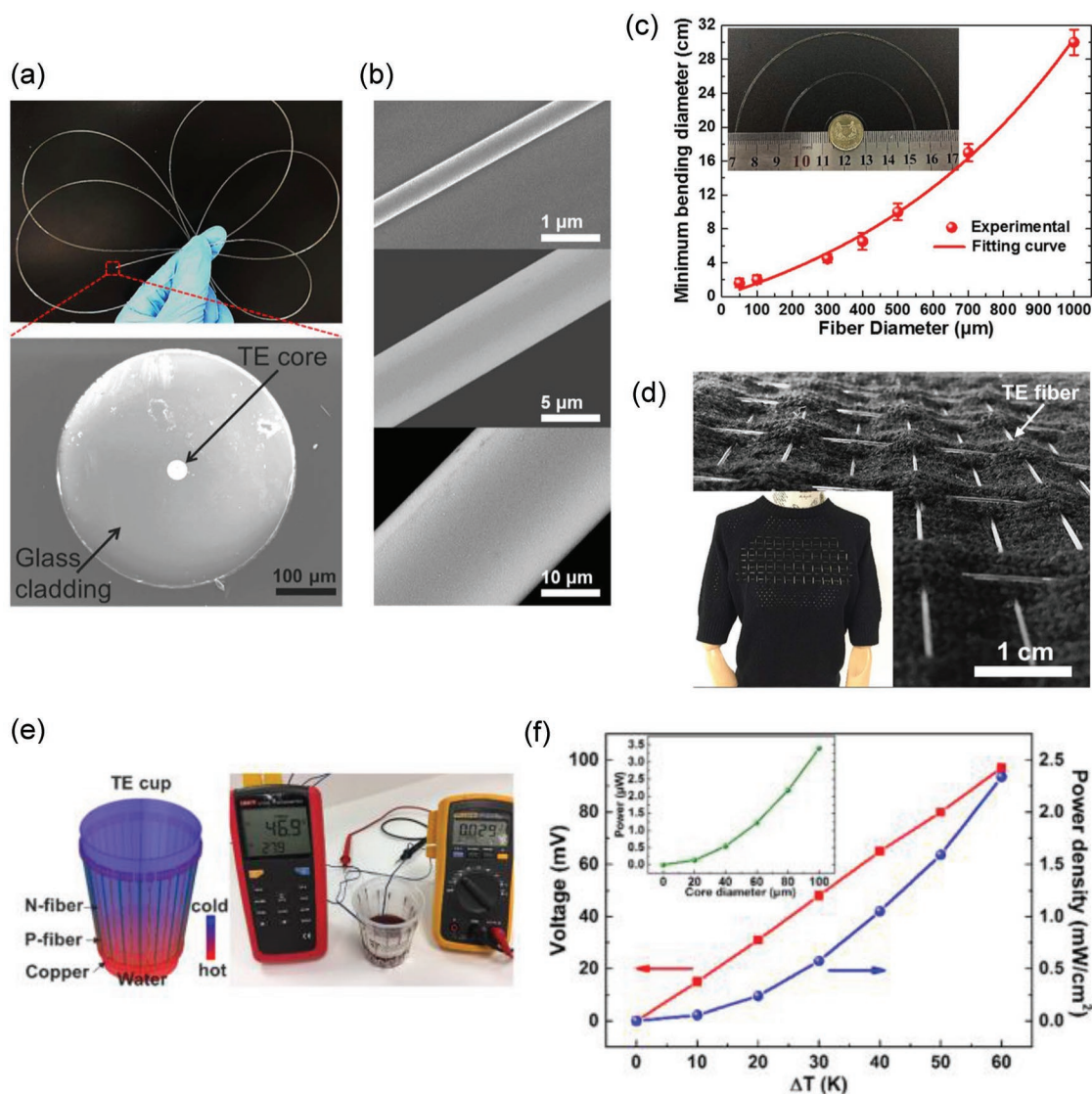


**Figure 14.** a) Single TE fiber with a length of one meter showing good flexibility. Below is its cross-sectional SEM image. b) SEM images of drawn TE fiber cores with the diameter from nano to microscale. c) Minimum bending diameters of TE fibers for different fiber diameters, and the inset exhibits bent TE fibers with diameters of 50, 400, and 500 μm, respectively. d) TE fibers are woven into a large-area fabric to construct a wearable TE device. e) Implementation of the TE fibers on a cup poured with hot water. f) Voltage and power density output from TE fibers for varying temperature differences. a–f) Reproduced with permission.<sup>[158]</sup> Copyright 2017, Elsevier.

objects with a temperature difference, such as a heated cup, to harvest a maximum  $2.34 \text{ mW cm}^{-2}$  level output power density for a temperature difference of  $60^\circ\text{C}$  (Figure 14e,f). This work bridged the gap between high-performance thermoelectric flexible fibers and their practical applications in energy harvesting as well as body cooling.

### 5.2.3. Piezoelectric Fibers

The piezoelectric effect is a reversible form of energy conversion. It can either convert mechanical loading into electricity or produce motion under an applied electric field. Power generation in this material is not only applicable to bodily movements but also different forms of pressure such as sound waves, wind,

and any other stimuli which induces mechanical stress. The first multimaterial piezoelectric fiber<sup>[22]</sup> integrated a piezoelectric P(VDF-TrFE) thin film sandwiched between two carbon based polymeric electrodes and encapsulated within a rigid polymer cladding. During thermal drawing, the melting of the piezoelectric domain and subsequent solidification resulted in the formation of piezoelectric  $\beta$ -phase. Confining the low viscosity crystalline piezoelectric domain between highly viscous electrodes alleviated the capillary break-up of the active material and thus resulted in uniform thickness across all material layers. Even though the fiber was exploited for acoustic transduction from kilohertz to megahertz frequencies, the conversion efficiency was limited and could not be utilized for power generation purposes. Exploring new designs like increasing the area of the active domain might enable efficient energy harvesting



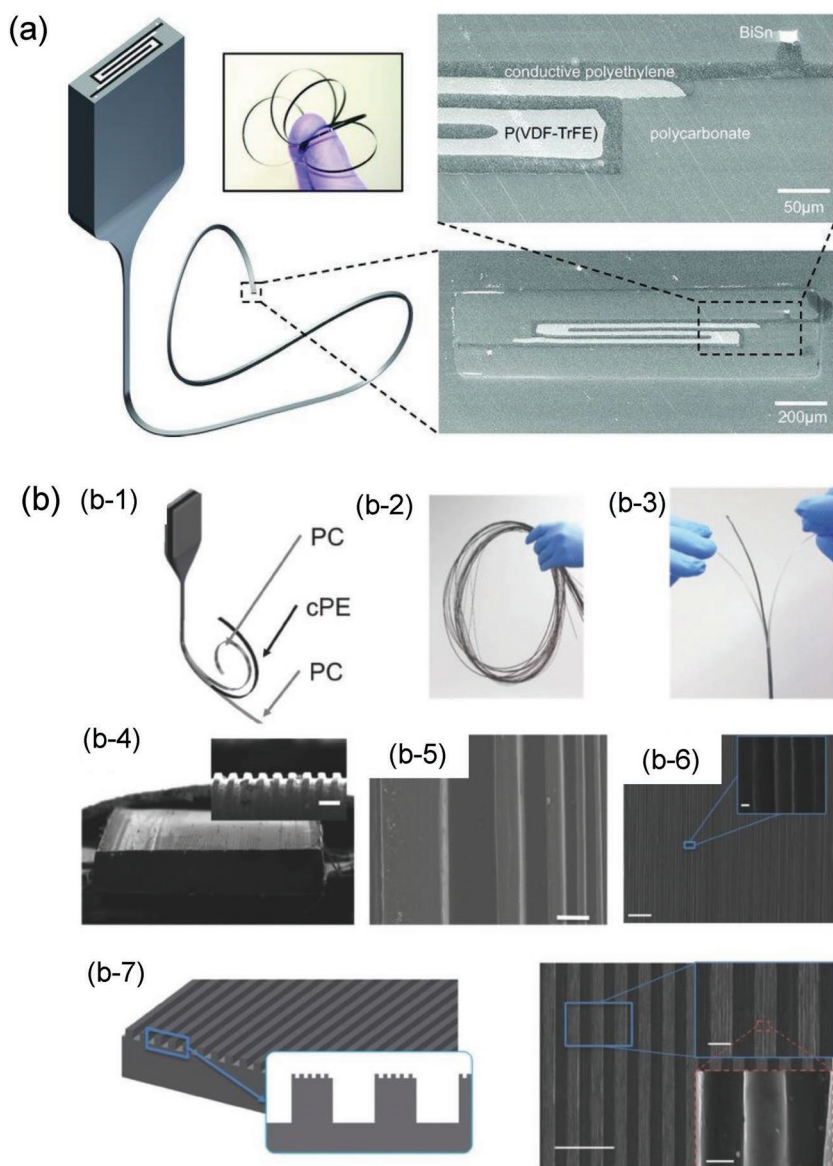


**Figure 15.** a) Multimaterial piezoelectric fiber. The schematic shows thermal drawing of a preform into the piezoelectric fiber. SEM micrograph shows the fiber cross-section where the multilayer piezoelectric domains are contacted by multilayer electrodes. Reproduced with permission.<sup>[22]</sup> Copyright 2012, Wiley-VCH. b) Micro- and nanoscale texture on the surface of polymeric fibers. b-1) Schematic of preform-to-fiber draws highlighting the separation between the different textured layers. b-2) Picture of extended length of a fiber ribbon. b-3) Picture of the peeling-off process. b-4) SEM image of a microscale textured ribbon. Inset shows the magnification at its surface. Scale bar: 15 μm. b-5) SEM image of the top view of microscale textured fibers with textures of different height and width (scale bar: 10 μm). b-6) SEM top view of a nanoscale textured ribbon with a square shape (scale bar: 10 μm) with a zoom-in image (inset scale bar: 200 nm). b-7) (left) Schematic and (right) SEM image of a double-textured ribbon (scale bar: 100 μm). The top inset shows its magnification (scale bar: 20 μm) and the bottom inset shows a further magnification (scale bar: 1 μm). b) Reproduced with permission.<sup>[126]</sup> Copyright 2017, Wiley-VCH.

capabilities. As such, a folded structure was introduced into another piezoelectric fiber, as shown in **Figure 15a**. The folded interdigitated fiber enabled a folded piezo-domain contacted by a multilayer electrode. The increased effective area in this new design allowed for an enhancement in the performance of piezoelectric fibers. Coherent interference and beam steering

capabilities were achieved using two- and four-fiber phased arrays. Later, Lu et al.<sup>[159]</sup> reported an all-polymer flexible piezoelectric fiber that exploited a similar multilayer design. The fiber features a hollow polycarbonate core surrounded by a spiral multilayer cladding consisting of alternating layers of piezoelectric nanocomposites and conductive polymer. Indeed, piezoelectric response was increased. The fibers exhibited high output voltage of up to 6 V under moderate bending, and they showed excellent durability in a cyclic bend-release test. The piezoelectric fibers were then weaved into textiles with high power generation demonstrated.

#### 5.2.4. Triboelectric Fibers

The triboelectric effect relies on surface electrification of two different materials rubbing against each other, resulting in one surface being charged positively and another negatively. While this effect is often a nuisance, triboelectricity has recently been successfully demonstrated for energy generation purposes.<sup>[160]</sup>

Triboelectricity in garments can be based on three different interfaces—1) fiber–fiber interactions, 2) fiber–skin interactions, and 3) in-fiber material interactions. First, when fibers of two different surface materials spatially meet on the crossing of woven fabric, friction-induced electricity can be created. In addition, the large surface area of fiber–fiber interactions is advantageous toward expanding the total triboelectricity generation. Surface engineering to increase the amount of interacting surface area on individual fibers could help maximize triboelectricity generation. Thermally drawn surface engineered fibers can be designed with micro or nanoscale texture on the polymer fiber surface using a recently developed fiber surface patterning technique.<sup>[126,161]</sup> As shown in **Figure 15b**, macroscopic patterns are first created in the preform using either laser patterning or mechanical milling approaches. In order to prevent the thermal reflow driven by the surface tension of the polymer and accelerated by the curvature of the patterns, a sacrificial polymer, having low miscibility with the patterned polymer, is interfaced with

the patterned polymer. This allows for the drastic decrease in surface tension leading to a long reflow time scale of the pattern. With this strategy, micro- and nanoscale texture with hierarchical structures spanning a wide range of feature sizes were produced both on the fiber surface and within the fiber. Triboelectric nanogenerators working in the vertical contact-separation

mode, the lateral sliding mode, the single-electrode mode or the free-standing mode fabricated using fibers with micro- and nanoscale patterns exhibit significantly improved energy conversion efficiency.<sup>[162]</sup> Second, natural friction with human skin generates electricity. This is familiar to us as static electricity. Skin can be positively charged when contacted with different kinds of polymers and could function as an efficient second material of the triboelectric system. Third, two different materials within the fiber itself can interact with each other upon mechanical agitation. For instance, as described in the earlier section, Nguyen-Dang et al.<sup>[86]</sup> created a fiber with electrode domains that were spatially separated by an air gap and could be electrically contacted with a moving mechanical force. This study shows that integration of cantilever-like structures with freely moving functional domains within multimaterial fibers

is feasible, paving the way for the development of in-fiber multimaterial triboelectric device.

## 6. Smart Fibers toward Computing Applications

To date, most thermally drawn fibers are focused on achieving disparate sensing functionalities and several forms of feedback such as light-emitting or actuation. An intriguing and important functionality that has yet to be fully explored is an in-fiber control system that regulates all sensory and feedback signals. In short, “smart” fibers, that are able to automatically process input and give output based on their stored memory, can be the bridge between sensing and feedback to enable applications<sup>[163,164]</sup> in computing, healthcare, and robotics. A simple example is a shape memory fiber that outputs different

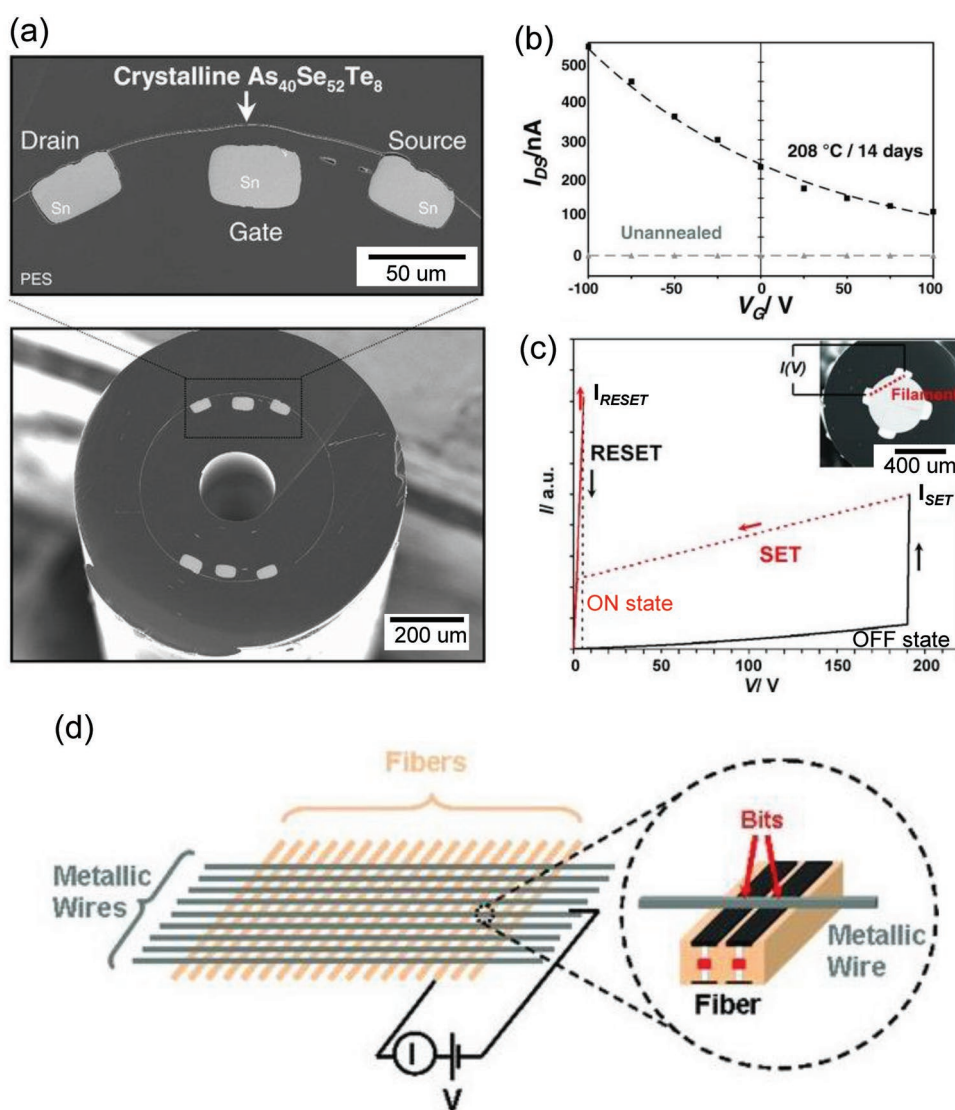


**Figure 16.** a) SEM images of the fiber field-effect device illustrating the Sn gate, source, and drain. The channel is made up of a crystalline AST thin film. b) Channel current versus gate voltage for an un-annealed AST film that is in its amorphous state and an AST film annealed at 208 °C for 14 days.  $V_{ds}$  is applied at 20 V. a,b) Reproduced with permission.<sup>[69]</sup> Copyright 2010, Wiley-VCH. c) Changes in the current–voltage as the ovonic memory-switching fiber undergo a SET/RESET operation. Inset shows the SEM cross section of the GAST fiber. d) Schematic of a fabric array consisting of GAST fibers with exposed electrodes arranged in a cross-bar array to increase memory space. c,d) Reproduced with permission.<sup>[165]</sup> Copyright 2011, Wiley-VCH.

configurations based on its programmed shapes at different temperatures. While a shape memory alloy changes shapes with a thermal input, it is important to investigate fibers that operate akin to a computer, giving millions of programmed outputs based on different electronic inputs. Preliminary work toward such a vision includes an in-fiber field-effect transistor<sup>[69]</sup>—an electronic device that is essential in computers. The in-fiber transistor structure consists of a p-type crystalline  $\text{As}_{40}\text{Se}_{52}\text{Te}_8$  semiconducting thin film as the channel, a Sn source/drain, and a Sn gate separated from the channel by a PES dielectric layer (Figure 16a). The basic operation of this in-fiber transistor is shown by the increase in channel conductance as the gate bias varies from 0 to  $-100$  V (Figure 16b). The required gate bias to attain a 100% ON–OFF current ratio is 75 V. While the voltage required for current modulation is still too high for practical use, this work represents the first step toward integrated digital circuitry in fibers.

In another work, phase change materials are harnessed to produce ovonic memory switching capabilities in fibers. Danto et al.<sup>[165]</sup> made use of  $\text{Ge}_{22}\text{As}_{18}\text{Se}_{15}\text{Te}_{45}$  (GAST) glass, which changes phases reversibly between highly resistive amorphous to highly conductive crystalline states with the application of voltage pulses. By applying a high voltage across Zn–Sn electrodes which interfaces GAST glass, the fiber transitions from an OFF (high resistance) to ON (low resistance) state. The mechanism by which this reversible change can happen is the injection of charged carriers into defect states.<sup>[166–168]</sup> This process enables a high current to pass through the GAST glass, resulting in Joule heating that leads to a rapid temperature increase for nucleation and growth of the crystal phase. To reset the ON state to the OFF state, the crystallized phase can first be reheated by applying another round of high voltage, and later quenched quickly to form the amorphous state. Both the crystalline and amorphous phases are stable even as the voltage is removed, so the in-fiber memory can be described to be nonvolatile. It is noted that the voltage threshold to switch the fiber from OFF to ON state is 190 V (Figure 16c). To further improve the power consumption, different chalcogenide glass compositions can be explored. In addition, the memory size is still constrained to a single bit per fiber. To increase the memory size for practical in-fiber computing applications, multiple fibers with surface-exposed electrodes can be arranged in a cross-hatched architecture to create a 2D grid of addressable interconnects with the memory density dependent on the density of interconnects (Figure 16d).

## 7. Conclusion and Outlook

Fibers, ancient yet largely underdeveloped forms, are evolving into functional electronic devices and smart systems over the past few decades. Tremendous efforts have been put into developing different methods toward fiber electronics fabrication. These technologies include, but are not limited to: 1) coating<sup>[169,170]</sup> (such as dip coating, spin coating, doctor blading); 2) spinning<sup>[171,172]</sup> (such as wet spinning, dry spinning, melt spinning and electrospinning); 3) deposition<sup>[173,174]</sup> (such as electrodeposition, electroless deposition, sputtering,

physical vapor deposition, chemical vapor deposition); 4) printing<sup>[175]</sup> (such as screen printing, inkjet printing, 3D printing, roll-to-roll printing); 5) physical integration<sup>[176–178]</sup> (such as twisting, weaving, braiding, convolution and wrapping). Owing to the simplicity, flexibility and especially the versatile capabilities in processing different materials by these approaches, a wide range of technologically important materials such as semiconducting nanowires, highly conductive metals, carbon nanotubes, perovskite, functional fluid, gels, or electrolyte, can be harnessed as active fiber materials—some of these materials are still restricted in the thermal drawing process due to the material's lack of ability for viscous flow. However, many of these techniques involve multiple process steps. In specific, key to ideal performance in fiber electronics is good interfacial bonding between different device building blocks, which necessitates for each process step to be highly optimized. Moreover, it remains technologically challenging for these techniques to scale to a large area. We will not review in full details of these technologies, but we refer the readers to a variety of relevant publications, including some state-of-the-art review articles<sup>[179–189]</sup> in the field.

Comparatively, the preform-to-fiber thermal drawing technique has emerged as a compelling platform for the fabrication of multimaterial fiber electronics. It exhibits several intriguing characteristics: 1) the macroscopic preform is constructed at the millimeter to centimeter scale, and thus desirable materials and structure can be precisely constructed. The subsequent thermal drawing leads to multimaterial fibers that maintain the preform cross-section with sophisticated structures; 2) Thermal co-drawing of different electronic materials with disparate electronic, optoelectronic, thermomechanical, rheological and acoustic properties results in fibers with complex functionalities which are described in this review; 3) the scalability is unparallel. Drawing a macroscopic preform produces potentially kilometers-long, thin fibers in a single step; 4) the feature size of active material can span three orders of magnitudes depending on the scale-down-ratio, hence well-defined nanoscale feature size can be achieved. The resulting fiber electronics can exhibit performance on par with their planar counterparts; 5) With a protective cladding material encapsulating the fiber electronics, thermally drawn fibers are water-resistant, enabling its practicality for washable fabrics. 6) As we discussed in the Section 4.3.2, it is also emerging as a versatile platform for utilizing and interconnecting high-performance commercialized materials or devices such as highly conductive microwires or semiconducting chips that cannot be co-drawn with typical fiber materials. Such breakthrough drastically extends the possibilities of fiber electronics.

Looking forward, we summarize several key points and lay out limitations of thermally drawn fibers in the following paragraphs to act as a guideline for scientists, researchers, and people in the industry to focus on and understand what is needed for future research and development specifically for the field of thermally drawn fiber electronics.

First, the database of materials compatible with thermal drawing is still limited. The constraints imposed on thermal drawing restrict the type of materials that can be processed and device architectures that can be fabricated. In order to overcome this limitation, first, in-depth understanding of the



thermomechanical and rheological properties of materials, such as the newly established rheological criterion,<sup>[87]</sup> is further required to expand the palette of thermally drawable materials. Next, it is necessary to develop new scalable post-drawing approaches (for example, materials deposition by HPCVD or materials structuring by annealing processes) to increase the range of functional materials that cannot be thermally drawn and to create new device functionalities in fibers that are comparable in performance to the mature thin-film technology. Combining the thermal draw technique with well-established commercialized materials and devices of microscale dimensions can also enable fibers of increased functionalities and performances.<sup>[35]</sup> In addition, the thermal drawing process is currently tuned by two inputs: the temperature and capstan speed. Introducing new stimuli during the fiber draw such as mechanical agitation or rotation can produce in situ structural changes to bring about novel fiber architectures.

Second, the fundamental aspects of microstructural formation of thermally drawn in-fiber materials as well as the interplay between its microstructure and properties are still poorly understood. This leads to limited optical, electronic, and optoelectronic performance. Improving the materials' microstructure would give rise to an enhancement of sensitivity to unveil many new fiber applications and enable the practical implementation of fiber electronics. For example, as a real-world application, highly touch-sensitive conformal fibers or fabrics can be used in the robotics industry as a robot-interfaced sensor that mimics the tactile sensing capabilities of the human skin for feeling and gripping objects.

Third, most fiber devices exhibit a single function. Monolithic integration of multiple functionalities into a single fiber remains a significant challenge. Increasing the density of devices integrated in a single fiber requires the feature size of active materials in fibers to be scaled down as small as possible while maintaining their functionalities. To address this issue, novel materials with ideal rheological properties,<sup>[190–192]</sup> that retain their functional features when scaled to lower dimensions, can be further investigated. With the increase in thermally drawable materials and new fabrication approaches, we envision that a single strand of fiber will encompass highly sophisticated fiber architectures—both within its cross-section and along its length—to exhibit a multitude of electronic functionalities, scaling in capabilities analogously to Moore's Law.

## Acknowledgements

G.L. and W.Y. contributed equally to this work. This work was supported in part by the National Science Foundation under the Materials Research Science and Engineering Center (MRSEC) program (Award number DMR-1419807) and in part by the US Army Research Laboratory and the US Army Research Office through the Institute for Soldier Nanotechnologies, under contract number W911NF-13-D-0001.

## Conflict of Interest

The authors declare no conflict of interest.

## Keywords

biomedicine, electronics, energy, multimaterial fibers, sensing

Received: July 30, 2019

Revised: September 6, 2019

Published online:

- [1] G. P. Agrawal, *Fiber-Optic Communication Systems*, John Wiley & Sons, Inc., Hoboken, NJ, USA **2011**.
- [2] R. Ramaswami, K. N. Sivarajan, G. H. Sasaki, *Optical Networks: A Practical Perspective*, Elsevier, Amsterdam **2010**.
- [3] G. T. Webb, P. J. Vardanega, N. A. Hoult, P. R. A. Fidler, P. J. Bennettand, C. R. Middleton, *J. Bridge Eng.* **2017**, *22*, 05017002.
- [4] F. Xiao, J. L. Hulse, R. Balasubramanian, *Struct. Control Health Monit.* **2017**, *24*, e2020.
- [5] Z. Zhou, J. P. He, M. H. Huang, J. He, J. P. Ou, G. D. Chen, *Proc. SPIE* **2010**, *7649*, 764908.
- [6] N. Mohamed, I. Jawhar, J. Al-Jaroodi, L. R. Zhang, *Sensors* **2011**, *11*, 10738.
- [7] G. Keiser, F. Xiong, Y. Cui, P. P. Shum, *J. Biomed. Opt.* **2014**, *19*, 080902.
- [8] S. Shabahang, S. Kim, S. H. Yun, *Adv. Funct. Mater.* **2018**, *28*, 1706635.
- [9] A. G. Mignani, F. Baldini, *Rep. Prog. Phys.* **1996**, *59*, 1.
- [10] J. I. Peterson, G. G. Vurek, *Science* **1984**, *224*, 123.
- [11] Q. Zhang, D. J. Roach, L. Geng, H. Chen, H. J. Qi, D. Fang, *Smart Mater. Struct.* **2018**, *27*, 035019.
- [12] S. Arumugam, Y. Li, S. Senthilarasu, R. Torah, A. L. Kanibolotsky, A. R. Inigo, P. J. Skabara, S. P. Beeby, *J. Mater. Chem. A* **2016**, *4*, 5561.
- [13] E. Torres Alonso, D. P. Rodrigues, M. Khetani, D.-W. Shin, A. De Sanctis, H. Joulie, I. de Schrijver, A. Baldycheva, H. Alves, A. I. S. Neves, S. Russo, M. F. Craciun, *npj Flexible Electron.* **2018**, *2*, 25.
- [14] J. Lee, J. Yoon, H. G. Kim, S. Kang, W. S. Oh, H. Algadi, S. Al-Sayari, B. Shong, S. H. Kim, H. Kim, T. Lee, H. B. R. Lee, *NPG Asia Mater.* **2016**, *8*, e331.
- [15] S. Seyedin, J. M. Razal, P. C. Innis, G. G. Wallace, *Smart Mater. Struct.* **2016**, *25*, 035015.
- [16] B. Zhang, F. Kang, J.-M. Tarascon, J.-K. Kim, *Prog. Mater. Sci.* **2016**, *76*, 319.
- [17] A. F. Abouraddy, M. Bayindir, G. Benoit, S. D. Hart, K. Kuriki, N. Orf, O. Shapira, F. Sorin, B. Temelkuran, Y. Fink, *Nat. Mater.* **2007**, *6*, 336.
- [18] M. Bayindir, A. F. Abouraddy, F. Sorin, J. Viens, J. D. Joannopoulos, Y. Fink, in *Conf. Lasers Electro-Optics (CLEO) Vol. 3*, IEEE, Piscataway, NJ, USA **2005**, pp. 1686–1687.
- [19] M. Bayindir, F. Sorin, A. F. Abouraddy, J. Viens, S. D. Hart, J. D. Joannopoulos, Y. Fink, *Nature* **2004**, *431*, 826.
- [20] M. Bayindir, A. E. Abouraddy, J. Arnold, J. D. Joannopoulos, Y. Fink, *Adv. Mater.* **2006**, *18*, 845.
- [21] A. Gumennik, A. M. Stolyarov, B. R. Schell, C. Hou, G. Lestoquoy, F. Sorin, W. McDaniel, A. Rose, J. D. Joannopoulos, Y. Fink, *Adv. Mater.* **2012**, *24*, 6005.
- [22] N. Chocat, G. Lestoquoy, Z. Wang, D. M. Rodgers, J. D. Joannopoulos, Y. Fink, *Adv. Mater.* **2012**, *24*, 5327.
- [23] T. Khudiyev, J. Clayton, E. Levy, N. Chocat, A. Gumennik, A. M. Stolyarov, J. Joannopoulos, Y. Fink, *Nat. Commun.* **2017**, *8*, 1435.
- [24] S. Egusa, Z. Wang, N. Chocat, Z. M. Ruff, A. M. Stolyarov, D. Shemuly, F. Sorin, P. T. Rakich, J. D. Joannopoulos, Y. Fink, *Nat. Mater.* **2010**, *9*, 643.

- [25] S. D. Hart, G. R. Maskaly, B. Temelkuran, P. H. Prideaux, J. D. Joannopoulos, Y. Fink, *Science* **2002**, 296, 510.
- [26] B. Temelkuran, S. D. Hart, G. Benoit, J. D. Joannopoulos, Y. Fink, *Nature* **2002**, 420, 650.
- [27] G. Tao, A. M. Stolyarov, A. F. Abouraddy, *Int. J. Appl. Glass Sci.* **2012**, 3, 349.
- [28] J. Eggers, E. Villermaux, *Rep. Prog. Phys.* **2008**, 71, 036601.
- [29] J. J. Kaufman, G. Tao, S. Shabahang, E.-H. Banaei, D. S. Deng, X. Liang, S. G. Johnson, Y. Fink, A. F. Abouraddy, *Nature* **2012**, 487, 463.
- [30] S. Shabahang, G. Tao, J. J. Kaufman, Y. Qiao, L. Wei, T. Bouchenot, A. P. Gordon, Y. Fink, Y. Bai, R. S. Hoy, A. F. Abouraddy, *Nature* **2016**, 534, 529.
- [31] L. Rayleigh, *Proc. R. Soc. London* **1879**, 29, 71.
- [32] A. Gumennik, L. Wei, G. Lestoquoy, A. M. Stolyarov, X. Jia, P. H. Rekemeyer, M. J. Smith, X. Liang, B. J.-B. Grena, S. G. Johnson, S. Gradečak, A. F. Abouraddy, J. D. Joannopoulos, Y. Fink, *Nat. Commun.* **2013**, 4, 2216.
- [33] J. Zhang, K. Li, T. Zhang, P. J. S. Buenconsejo, M. Chen, Z. Wang, M. Zhang, Z. Wang, L. Wei, *Adv. Funct. Mater.* **2017**, 27, 1703245.
- [34] M. Rein, E. Levy, A. Gumennik, A. F. Abouraddy, J. Joannopoulos, Y. Fink, *Nat. Commun.* **2016**, 7, 12807.
- [35] M. Rein, V. D. Favrod, C. Hou, T. Khudiyev, A. Stolyarov, J. Cox, C. C. Chung, C. Chhav, M. Ellis, J. Joannopoulos, Y. Fink, *Nature* **2018**, 560, 214.
- [36] T. Das Gupta, L. Martin-Monier, W. Yan, A. Le Bris, T. Nguyen-Dang, A. G. Page, K.-T. Ho, F. Yesilköy, H. Altug, Y. Qu, F. Sorin, *Nat. Nanotechnol.* **2019**, 14, 320.
- [37] T. Das Gupta, L. Martin-Monier, W. Yan, A. Le Bris, T. D. Nguyen, A. Page, Y. Qu, F. Sorin, *CLEO: Science and Innovations* **2018**, STh11.5.
- [38] F. Sorin, A. G. Page, L. Martin-Monier, Y. Qu, T. Das Gupta, W. Yan, T. Nguyen-Dang, *CLEO Pacific Rim* **2018**, W1C.2.
- [39] G. Tang, Q. Qian, X. Wen, X. Chen, W. Liu, M. Sun, Z. Yang, *Opt. Express* **2015**, 23, 23624.
- [40] K. Huang, G. Tang, Q. Luo, G. Qian, L. Yang, F. Yuan, Z. Shi, Q. Qian, Z. Yang, *Mater. Res. Bull.* **2018**, 100, 382.
- [41] W. Yan, Y. Qu, T. Das Gupta, A. Darga, D. T. Nguyen, A. G. Page, M. Rossi, M. Ceriotti, F. Sorin, *Adv. Mater.* **2017**, 29, 1700681.
- [42] F. Sorin, W. Yam, M. Volpi, A. G. Page, T. Nguyen-Dang, Y. Qu, *Proc. SPIE* **2017**, 10194, 1019407.
- [43] S. Donati, *Meas. Sci. Technol.* **2002**, 12, 653.
- [44] M. Bayindir, A. F. Abouraddy, F. Sorin, J. D. Joannopoulos, Y. Fink, *Opt. Photonics News* **2004**, 15, 24.
- [45] A. F. Abouraddy, O. Shapira, M. Bayindir, J. Arnold, F. Sorin, D. S. Hinczewski, J. D. Joannopoulos, Y. Fink, *Nat. Mater.* **2006**, 5, 532.
- [46] F. Sorin, G. Lestoquoy, S. Danto, J. D. Joannopoulos, Y. Fink, *Opt. Express* **2010**, 18, 24264.
- [47] F. Sorin, A. F. Abouraddy, N. Orf, O. Shapira, J. Viens, J. Arnold, J. D. Joannopoulos, Y. Fink, *Adv. Mater.* **2007**, 19, 3872.
- [48] F. Sorin, O. Shapira, A. F. Abouraddy, M. Spencer, N. D. Orf, J. D. Joannopoulos, Y. Fink, *Nano Lett.* **2009**, 9, 2630.
- [49] N. Healy, U. Gibson, A. C. Peacock, *Semicond. Sci. Technol.* **2018**, 33, 023001.
- [50] L. Wei, C. Hou, E. Levy, G. Lestoquoy, A. Gumennik, A. F. Abouraddy, J. D. Joannopoulos, Y. Fink, *Adv. Mater.* **2016**, 29, 1603033.
- [51] S. Shabahang, J. J. Kaufman, D. S. Deng, A. F. Abouraddy, *Appl. Phys. Lett.* **2011**, 99, 57.
- [52] G. Tao, J. J. Kaufman, S. Shabahang, R. Rezvani Naraghi, S. V. Sukhov, J. D. Joannopoulos, Y. Fink, A. Dogariu, A. F. Abouraddy, *Proc. Natl. Acad. Sci. USA* **2016**, 113, 6839.
- [53] A. Gumennik, E. C. Levy, B. Grena, C. Hou, M. Rein, A. F. Abouraddy, J. D. Joannopoulos, Y. Fink, *Proc. Natl. Acad. Sci. USA* **2017**, 114, 7240.
- [54] M. Fokine, A. Theodosiou, S. Song, T. Hawkins, J. Ballato, K. Kalli, U. J. Gibson, *Opt. Mater. Express* **2017**, 7, 1589.
- [55] D. S. Deng, N. D. Orf, A. F. Abouraddy, A. M. Stolyarov, J. D. Joannopoulos, H. A. Stone, Y. Fink, *Nano Lett.* **2008**, 8, 4265.
- [56] D. S. Deng, J. C. Nave, X. Liang, S. G. Johnson, Y. Fink, *Opt. Express* **2011**, 19, 16273.
- [57] B. Xu, M. Li, F. Wang, S. G. Johnson, Y. Fink, D. Deng, *Phys. Rev. Fluids* **2019**, 4, 073902.
- [58] J. R. Sparks, P. J. A. Sazio, V. Gopalan, J. V. Badding, *Annu. Rev. Mater. Res.* **2013**, 43, 527.
- [59] R. He, P. J. A. Sazio, A. C. Peacock, N. Healy, J. R. Sparks, M. Krishnamurthi, V. Gopalan, J. V. Badding, *Nat. Photonics* **2012**, 6, 174.
- [60] R. He, T. D. Day, M. Krishnamurthi, J. R. Sparks, P. J. A. Sazio, V. Gopalan, J. V. Badding, *Adv. Mater.* **2013**, 25, 1461.
- [61] F. A. Martinsen, B. K. Smeltzer, M. Nord, T. Hawkins, J. Ballato, U. J. Gibson, *Sci. Rep.* **2014**, 4, 6283.
- [62] C. Hou, X. Jia, L. Wei, A. M. Stolyarov, O. Shapira, J. D. Joannopoulos, Y. Fink, *Nano Lett.* **2013**, 13, 975.
- [63] N. D. Orf, O. Shapira, F. Sorin, S. Danto, M. A. Baldo, J. D. Joannopoulos, Y. Fink, *Proc. Natl. Acad. Sci. USA* **2011**, 108, 4743.
- [64] J. R. Sparks, R. He, N. Healy, M. Krishnamurthi, A. C. Peacock, P. J. A. Sazio, V. Gopalan, J. V. Badding, *Adv. Mater.* **2011**, 23, 1647.
- [65] W. Yan, A. Page, T. Nguyen-Dang, Y. Qu, F. Sordo, L. Wei, F. Sorin, *Adv. Mater.* **2019**, 31, 1802348.
- [66] W. Yan, *Ph.D. Thesis*, École Polytechnique Fédérale de Lausanne, Lausanne, Switzerland **2017**.
- [67] W. Yan, T. Nguyen-Dang, C. Cayron, T. Das Gupta, A. G. Page, Y. Qu, F. Sorin, *Opt. Mater. Express* **2017**, 7, 1388.
- [68] W. Yan, Y. Qu, D. T. Nguyen, M. Volpi, A. G. Page, F. Sorin, *Asia Communications and Photonics (OSA)* **2016**, AF3A.3.
- [69] S. Danto, F. Sorin, N. D. Orf, Z. Wang, S. A. Speakman, J. D. Joannopoulos, Y. Fink, *Adv. Mater.* **2010**, 22, 4162.
- [70] N. Gupta, C. McMillen, R. Singh, R. Podila, A. M. Rao, T. Hawkins, P. Foy, S. Morris, R. Rice, K. F. Poole, L. Zhu, J. Ballato, *J. Appl. Phys.* **2011**, 110, 093107.
- [71] S. Morris, C. McMillen, T. Hawkins, P. Foy, R. Stolen, J. Ballato, R. Rice, *J. Cryst. Growth* **2012**, 352, 53.
- [72] C. McMillen, G. Brambilla, S. Morris, T. Hawkins, P. Foy, N. Broderick, E. Koukharenko, R. Rice, J. Ballato, *Opt. Mater.* **2012**, 35, 93.
- [73] S. Shaudhuri, J. R. Sparks, X. Ji, M. Krishnamurthi, L. Shen, N. Healy, A. C. Peacock, V. Gopalan, J. V. Badding, *ACS Photonics* **2016**, 3, 378.
- [74] S. Peng, G. Tang, K. Huang, Q. Qian, D. Chen, Q. Zhang, Z. Yang, *Opt. Express* **2017**, 7, 1804.
- [75] D. S. Deng, N. D. Orf, S. Danto, A. F. Abouraddy, J. D. Joannopoulos, Y. Fink, *Appl. Phys. Lett.* **2010**, 96, 023102.
- [76] Y. F. Ranz, A. F. J. R. Unge, H. R. En, N. H. Ealy, K. I. Gnatyev, M. J. Ones, T. H. Awkins, J. B. Allato, U. J. G. Ibsen, A. C. P. Eacock, *Opt. Mater. Express* **2017**, 7, 2055.
- [77] A. Watillon, J. Dauchot, *J. Colloid Interface Sci.* **1968**, 27, 507.
- [78] D. A. Coucheron, M. Fokine, N. Patil, D. W. Breiby, O. T. Buset, N. Healy, A. C. Peacock, T. Hawkins, M. Jones, J. Ballato, U. J. Gibson, *Nat. Commun.* **2016**, 7, 13265.
- [79] X. Ji, S. Lei, S.-Y. Yu, H. Y. Cheng, W. Liu, N. Poilvert, Y. Xiong, I. Dabo, S. E. Mohny, J. V. Badding, V. Gopalan, *ACS Photonics* **2017**, 4, 85.
- [80] X. Ji, R. L. Page, S. Chaudhuri, W. Liu, S. Y. Yu, S. E. Mohny, J. V. Badding, V. Gopalan, *Adv. Opt. Mater.* **2016**, 5, 1600592.

- [81] Z. Zhao, Y. Mao, L. Ren, J. Zhang, N. Chen, T. Wang, *Opt. Mater. Express* **2019**, 9, 1333.
- [82] W. Yan, T. Das Gupta, I. Richard, F. Sorin, *CLEO: Science and Innovations* **2018**, SF2K.4.
- [83] W. Yan, A. Burgos-Caminal, T. Das Gupta, J.-E. Moser, F. Sorin, *J. Phys. Chem. C* **2018**, 122, 25134.
- [84] Y. Xia, P. Yang, Y. Sun, Y. Wu, B. Mayers, B. Gates, Y. Yin, F. Kim, H. Yan, *Adv. Mater.* **2003**, 15, 353.
- [85] A. M. Stolyarov, A. Gumennik, W. McDaniel, O. Shapira, B. Schell, F. Sorin, K. Kuriki, G. Benoit, A. Rose, J. D. Joannopoulos, Y. Fink, *Opt. Express* **2012**, 20, 12407.
- [86] T. Nguyen-Dang, G. A. Page, Y. Qu, M. Volpi, W. Yan, F. Sorin, *J. Phys. D: Appl. Phys.* **2017**, 50, 144001.
- [87] Y. Qu, D. T. Nguyen, A. G. Page, W. Yan, T. Das Gupta, G. M. Rotaru, R. Rossi, V. Favrod, N. Bartolomei, F. Sorin, *Adv. Mater.* **2018**, 30, 1707251.
- [88] F. Sorin, Y. Qu, M. Volpi, W. Yan, D. T. Nguyen, A. Page, *US Patent*, 20190047240A1, **2017**.
- [89] N. Bartolomei, Y. Qu, T. Nguyen Dang, W. Yan, A. G. Page, T. Das Gupta, A. Leber, F. Sorin, *Proc. SPIE* **2019**, 10872.
- [90] Y. Qu, N. Bartolomei, M. Lagier, T. Nguyen-Dang, A. G. Page, W. Yan, T. Das Gupta, F. Sorin, *Optical Fiber Sensors* **2018**, ThE66.
- [91] Y. Qu, T. Nguyen-Dang, A. G. Page, W. Yan, T. Das Gupta, G. M. Rotaru, R. M. Rossi, V. D. Favrod, N. Bartolomei, F. Sorin, *International Flexible Electronics Technology* **2018**.
- [92] Y. Qu, N. Bartolomei, M. Lagier, T. Nguyen-Dang, A. G. Page, W. Yan, T. Das Gupta, F. Sorin, *Specialty Optical Fibers* **2018**, SoW1H.3.
- [93] F. Sordo, E.-R. Janecek, Y. Qu, V. Michaud, F. Stellacci, J. Engmann, T. J. Wooster, F. Sorin, *Adv. Mater.* **2019**, 31, 1807282.
- [94] A. Chortos, J. Liu, Z. Bao, *Nat. Mater.* **2016**, 15, 937.
- [95] M. Kanik, S. Orguc, G. Varnavides, J. Kim, T. Benavides, D. Gonzalez, T. Akintilo, C. C. Tasan, A. P. Chandrakasan, Y. Fink, P. Anikeeva, *Science* **2019**, 365, 145.
- [96] C. Bartolozzi, L. Natale, F. Nori, G. Metta, *Nat. Mater.* **2016**, 15, 921.
- [97] L. Tian, H. Wang, X. Yu, A. C. Silva, Y. Yu, A. Koh, R. Oklu, A. Chempakasseril, H. Albadawi, J. Yuan, Y. Huang, R. Sun, P. Tian, J. A. Rogers, M. Salomao, M. Pharr, X. Ning, C. M. Lee, *Nat. Biomed. Eng.* **2018**, 2, 165.
- [98] A. A. M. Stolyarov, L. Wei, O. Shapira, F. Sorin, S. L. Chua, J. D. Joannopoulos, Y. Fink, *Nat. Photonics* **2012**, 6, 229.
- [99] S. Lv, B. Shanmugavelu, Y. Wang, Q. Mao, Y. Zhao, Y. Yu, J. Hao, Q. Zhang, J. Qiu, S. Zhou, *Adv. Opt. Mater.* **2018**, 6, 1800881.
- [100] G. Loke, R. Yuan, M. Rein, T. Khudiyev, Y. Jain, J. Joannopoulos, Y. Fink, *Nat. Commun.* **2019**, 10, 4010.
- [101] E. Boyden, *F1000 Biol. Rep.* **2011**, 3, 11.
- [102] S. Park, G. Loke, Y. Fink, P. Anikeeva, *Chem. Soc. Rev.* **2019**, 48, 1826.
- [103] A. Canales, X. Jia, U. P. Froriep, R. A. Koppes, C. M. Tringides, J. Selvidge, C. Lu, C. Hou, L. Wei, Y. Fink, P. Anikeeva, *Nat. Biotechnol.* **2015**, 33, 277.
- [104] S. Park, Y. Guo, X. Jia, H. K. Choe, B. Grena, J. Kang, J. Park, C. Lu, A. Canales, R. Chen, Y. S. Yim, G. B. Choi, Y. Fink, P. Anikeeva, *Nat. Neurosci.* **2017**, 20, 612.
- [105] C. Lu, S. Park, T. J. Richner, A. Derry, I. Brown, C. Hou, S. Rao, J. Kang, C. T. Mortiz, Y. Fink, P. Anikeeva, *Sci. Adv.* **2017**, 3, e1600955.
- [106] Y. Won, A. Kim, W. Yang, S. Jeong, J. Moon, *NPG Asia Mater.* **2014**, 6, e132.
- [107] S. B  fahy, S. Yunus, T. Pardo  n, P. Bertrand, M. Troosters, *Appl. Phys. Lett.* **2007**, 91, 141911.
- [108] C. Wang, W. Zheng, Z. Yue, C. O. Too, G. G. Wallace, *Adv. Mater.* **2011**, 23, 3580.
- [109] C. Yu, C. Masarapu, J. Rong, B. Q. M. Wei, H. Jiang, *Adv. Mater.* **2009**, 21, 4793.
- [110] J. Hao, J. Ruel, B. Coste, Y. Roudaut, M. Crest, P. Delmas, *Methods Mol. Biol.* **2013**, 998, 159.
- [111] D. S  nchez, U. Anand, J. Gorelik, C. D. Benham, C. Bountra, M. Lab, D. Klennerman, R. Birch, P. Anand, Y. Korchev, *J. Neurosci. Methods* **2007**, 159, 26.
- [112] S. Chanet, A. C. Martin, *Prog. Mol. Biol. Transl. Sci.* **2014**, 126, 317.
- [113] L. Huang, R. K. Korhonen, M. J. Turunen, M. A. J. Finnil  , *PeerJ* **2019**, 7, e6545.
- [114] C. E. Schmidt, J. B. Leach, *Annu. Rev. Biomed. Eng.* **2003**, 5, 293.
- [115] Z. L. Chen, W. M. Yu, S. Strickland, *Annu. Rev. Neurosci.* **2007**, 30, 209.
- [116] J. Noble, C. A. Munro, V. S. Prasad, R. Midha, *J. Trauma* **1998**, 45, 116.
- [117] K. Pawar, R. Mueller, M. Caioni, P. Prang, U. Bogdahn, W. Kunz, N. Weidner, *Acta Biomater.* **2011**, 7, 2826.
- [118] Stoyanova II, R. J. van Wezel, W. L. Rutten, *J. Neural Eng.* **2013**, 10, 066018.
- [119] J. S. Belkas, M. S. Shoichet, R. Midha, *Neurol. Res.* **2004**, 26, 151.
- [120] J. A. Hammarback, S. L. Palm, L. T. Furcht, P. C. Letourneau, *J. Neurosci. Res.* **1985**, 13, 213.
- [121] Y.-T. Kim, V. K. Haftel, S. Kumar, R. V. Bellamkonda, *Biomaterials* **2008**, 29, 3117.
- [122] D. Mortimer, T. Fothergill, Z. Pujic, L. J. Richards, G. J. Goodhill, *Trends Neurosci.* **2008**, 31, 90.
- [123] C. Bouzigues, D. Holcman, M. Dahan, *PLoS One* **2010**, 5, e9243.
- [124] S. Park, R. A. Koppes, U. P. Froriep, X. Jia, A. K. H. Achyuta, B. L. McLaughlin, P. Anikeeva, *Sci. Rep.* **2015**, 5, 9669.
- [125] R. A. Koppes, S. Park, T. Hood, X. Jia, N. Abdolrahim Poorheravi, A. H. Achyuta, Y. Fink, P. Anikeeva, *Biomaterials* **2016**, 81, 27.
- [126] T. Nguyen-Dang, A. C. de Luca, W. Yan, Y. Qu, A. G. Page, M. Volpi, T. Das Gupta, S. P. Lacour, F. Sorin, *Adv. Funct. Mater.* **2017**, 27, 1605935.
- [127] D. M. Thompson, A. N. Koppes, J. G. Hardy, C. E. Schmidt, *Annu. Rev. Biomed. Eng.* **2014**, 16, 397.
- [128] A. A. Al-Majed, C. M. Neumann, T. M. Brushart, T. Gordon, *J. Neurosci.* **2000**, 20, 2602.
- [129] A. N. Koppes, A. L. Nordberg, G. Paolillo, N. Goodsell, H. Darwish, L. Zhang, D. M. Thompson, *Tissue Eng., Part A* **2013**, 20, 494.
- [130] R. Yuan, J. Lee, H.-W. Su, E. Levy, T. Khudiyev, J. Voldman, Y. Fink, *Proc. Natl. Acad. Sci. USA* **2018**, 115, E10830.
- [131] B. Grena, J.-B. Alayrac, E. Levy, A. M. Stolyarov, J. D. Joannopoulos, Y. Fink, *Nat. Commun.* **2017**, 8, 364.
- [132] D. Shahriari, G. Loke, I. Tafel, S. Park, P. H. Chiang, Y. Fink, P. Anikeeva, *Adv. Mater.* **2019**, 31, 1902021.
- [133] E. A. Carvalho, A. P. Catarino, A. Rocha, O. Postolache, *2014 IEEE Int. Symp. Med. Meas. Appl.*, IEEE, Piscataway, NJ **2014**, pp. 1–6.
- [134] A. Pantelopoulou, N. G. Bourbakis, *IEEE Trans. Syst. Man Cybern. Part C Appl. Rev.* **2010**, 40, 1.
- [135] G. Loriga, N. Taccini, D. De Rossi, R. Paradiso, *2005 IEEE Eng. Med. Biol. 27th Annu. Conf.*, IEEE, Piscataway, NJ **2006**, pp. 7349–7352.
- [136] E. A. Tansey, C. D. Johnson, *Adv. Physiol. Educ.* **2015**, 39, 139.
- [137] Q. Li, L.-N. Zhang, X.-M. Tao, X. Ding, *Adv. Healthcare Mater.* **2017**, 6, 1601371.
- [138] P. J. Young, R. Bellomo, *Crit. Care* **2014**, 18, 109.
- [139] T. Oka, *Temperature* **2015**, 2, 368.
- [140] K. A. Herborn, J. L. Graves, P. Jerem, N. P. Evans, R. Nager, D. J. McCafferty, D. E. F. McKeegan, *Physiol. Behav.* **2015**, 152, 225.
- [141] A. E. Draghici, J. A. Taylor, *J. Physiol. Anthropol.* **2016**, 35, 22.
- [142] A. M. Ga  n-Calvo, J. Fajardo-L  pez, *Sci. Rep.* **2016**, 6, 21749.
- [143] A. Von Chong, M. Terosiet, A. Histace, O. Romain, *Microelectronics J.* **2018**, 88, 128.



- [144] Y. Khan, D. Han, A. Pierre, J. Ting, X. Wang, C. M. Lochner, G. Bovo, N. Yaacobi-Gross, C. Newsome, R. Wilson, A. C. Arias, *Proc. Natl. Acad. Sci. USA* **2018**, *115*, E11015.
- [145] O. Yossef Hay, M. Cohen, I. Nitzan, Y. Kasirer, S. Shahroorkarni, Y. Yitzhaky, S. Engelberg, M. Nitzan, *Sensors* **2018**, *18*, 3457.
- [146] J. Choi, R. Ghaffari, L. B. Baker, J. A. Rogers, *Sci. Adv.* **2018**, *4*, eaar3921.
- [147] R. W. Bullard, M. R. Banerjee, B. A. Mac Intyre, *Int. J. Biometeorol.* **1967**, *11*, 93.
- [148] V. Leonov, in *Wearable Monitoring Systems* (Eds: A. Bonfiglio, D. De Rossi), Springer Science and Business Media, LLC, Berlin, Germany **2011**, pp. 27–49.
- [149] M. D. Yadav, K. Dasgupta, A. W. Patwardhan, J. B. Joshi, *Ind. Eng. Chem. Res.* **2017**, *56*, 12407.
- [150] K. Koziol, J. Vilatela, A. Moissala, M. Motta, P. Cuniff, M. Sennett, A. Windle, *Science* **2007**, *318*, 1892.
- [151] M. Zhang, K. R. Atkinson, R. H. Baughman, *Science* **2004**, *306*, 1358.
- [152] B. Vigolo, A. Penicaud, C. Coulon, C. Sauder, R. Pailier, C. Journet, P. Bernier, P. Poulin, *Science* **2000**, *290*, 1331.
- [153] G. Lestoquoy, N. Chocat, Z. Wang, J. D. Joannopoulos, Y. Fink, *Appl. Phys. Lett.* **2013**, *102*, 152908.
- [154] J. Liu, M. A. G. Namboothiry, D. L. Carroll, *Appl. Phys. Lett.* **2007**, *90*, 063501.
- [155] T. Chen, S. Wang, Z. Yang, Q. Feng, X. Sun, L. Li, Z. S. Wang, H. Peng, *Angew. Chem., Int. Ed.* **2011**, *50*, 1815.
- [156] M. Culebras, C. M. Gómez, A. Cantarero, *Materials* **2014**, *6*, 6701.
- [157] G. J. Snyder, E. S. Toberer, *Nat. Mater.* **2008**, *7*, 105.
- [158] T. Zhang, K. Li, J. Zhang, M. Chen, Z. Wang, S. Ma, N. Zhang, L. Wei, *Nano Energy* **2017**, *41*, 35.
- [159] X. Lu, H. Qu, M. Skorobogatiy, *ACS Nano* **2017**, *11*, 2103.
- [160] F. R. Fan, Z. Q. Tian, Z. Lin Wang, *Nano Energy* **2012**, *1*, 328.
- [161] T. Khudiyev, C. Hou, A. M. Stolyarov, Y. Fink, *Adv. Mater.* **2017**, *29*, 1605868.
- [162] Z. L. Wang, J. Chen, L. Lin, *Energy Environ. Sci.* **2015**, *8*, 2250.
- [163] V. Koncar, *Smart Textiles and Their Applications*, Elsevier, Amsterdam, The Netherlands **2016**.
- [164] X. Tao, *Smart Fibres, Fabrics and Clothing*, Woodhead Publishing Limited, Sawston, Cambridge, UK **2001**.
- [165] S. Danto, Z. Ruff, Z. Wang, J. D. Joannopoulos, Y. Fink, *Adv. Funct. Mater.* **2011**, *21*, 1095.
- [166] M. Wuttig, N. Yamada, *Nat. Mater.* **2007**, *6*, 824.
- [167] S. Mondal, *Appl. Therm. Eng.* **2008**, *28*, 1536.
- [168] D. Adler, M. S. Shur, M. Silver, S. R. Ovshinsky, *J. Appl. Phys.* **1980**, *51*, 3289.
- [169] X. Li, J. Zhou, J. Zhang, M. Li, X. Bi, T. Liu, T. He, J. Cheng, F. Zhang, Y. Li, X. Mu, J. Lu, B. Wang, *Adv. Mater.* **2019**, *28*, 1903852.
- [170] J. Deng, W. Zhuang, L. Bao, X. Wu, J. Gao, B. Wang, X. Sun, H. Peng, *Carbon* **2019**, *149*, 63.
- [171] T. Huang, C. Wang, H. Yu, H. Wang, Q. Zhang, M. Zhu, *Nano Energy* **2014**, *14*, 226.
- [172] Z. Qi, H. Yu, Y. Chen, M. Zhu, *Mater. Lett.* **2009**, *63*, 415.
- [173] H. W. Lee, M. A. Schmidt, R. F. Russell, N. Y. Joly, H. K. Tyagi, P. Uebel, P. S. J. Russell, *Opt. Express* **2011**, *19*, 12180.
- [174] P. J. A. Sazio, A. Amezcua-Correa, C. E. Finlayson, J. R. Hayes, T. J. Scheidemantel, N. F. Baril, B. R. Jackson, D. J. Won, F. Zhang, E. R. Margine, V. Gopalan, V. H. Crespi, J. V. Badding, *Science* **2006**, *311*, 1583.
- [175] A. Frutiger, J. T. Muth, D. M. Vogt, Y. Mengüç, A. Campo, A. D. Valentine, C. J. Walsh, J. A. Lewis, *Adv. Mater.* **2015**, *27*, 2440.
- [176] J. Bae, M. K. Song, Y. J. Park, J. M. Kim, M. Liu, Z. L. Wang, *Angew. Chem., Int. Ed.* **2011**, *50*, 1683.
- [177] J. Zhong, Y. Zhang, Q. Zhong, Q. Hu, B. Hu, Z. L. Wang, J. Zhou, *ACS Nano* **2014**, *8*, 6273.
- [178] J. Deng, Y. Xu, S. He, P. Chen, L. Bao, Y. Hu, B. Wang, X. Sun, H. Peng, *Nat. Protoc.* **2017**, *12*, 1349.
- [179] W. Zeng, L. Shu, Q. Li, S. Chen, F. Wang, X. M. Tao, *Adv. Mater.* **2014**, *26*, 5310.
- [180] W. Weng, J. Yang, Y. Zhang, Y. Li, S. Yang, L. Zhu, M. Zhu, *Adv. Mater.* **2019**, 1902301.
- [181] K. Dong, X. Peng, Z. L. Wang, *Adv. Mater.* **2019**, 1902549.
- [182] B. Fang, D. Chang, Z. Xu, C. Gao, *Adv. Mater.* **2019**, 1902664.
- [183] Y. Jang, S. M. Kim, G. M. Spinks, S. J. Kim, *Adv. Mater.* **2019**, 1902670.
- [184] F. Mo, G. Liang, Z. Huang, H. Li, D. Wang, C. Zhi, *Adv. Mater.* **2019**, 1902151.
- [185] T. Xu, Z. Zhang, L. Qu, *Adv. Mater.* **2019**, 1901979.
- [186] X. Zhang, W. Lu, G. Zhou, Q. Li, *Adv. Mater.* **2019**, 1902028.
- [187] L. Huang, S. Lin, Z. Xu, H. Zhou, J. Duan, B. Hu, J. Zhou, *Adv. Mater.* **2019**, 1902034.
- [188] D. Chen, K. Jiang, T. Huang, G. Shen, *Adv. Mater.* **2019**, 1901806.
- [189] Y. Zhang, J. Ding, B. Qi, W. Tao, J. Wang, C. Zhao, H. Peng, J. Shi, *Adv. Funct. Mater.* **2019**, *29*, 1902834.
- [190] W. Yan, Y. Liu, Y. Zhu, S. Niu, *Int. J. Mater. Res.* **2011**, *102*, 435.
- [191] Y. Liu, Y. Zhu, F. Li, W. Yan, *Adv. Eng. Mater.* **2010**, *12*, 1131.
- [192] M. D. Dickey, *Adv. Mater.* **2017**, *29*, 1606425.